

# Extragalactic Fields Optimized for Adaptive Optics

Ivana Damjanov<sup>1</sup>, Roberto G. Abraham<sup>1</sup>, Karl Glazebrook<sup>2</sup>, Peter McGregor<sup>3</sup>, Francois Rigaut<sup>4</sup>, Patrick J. McCarthy<sup>5</sup>, Jarle Brinchmann<sup>6,7</sup>, Jean-Charles Cuillandre<sup>8</sup>, Yannick Mellier<sup>9</sup>, Henry Joy McCracken<sup>9</sup>, Patrick Hudelot<sup>9</sup>, David Monet<sup>10</sup>

## ABSTRACT

In this paper we present the coordinates of  $67\ 55' \times 55'$  patches of sky which have the rare combination of both high stellar surface density ( $\geq 0.5\ \text{arcmin}^{-2}$  with  $13 < R < 16.5\ \text{mag}$ ) and low extinction ( $E(B - V) \leq 0.1$ ). These fields are ideal for adaptive-optics based follow-up of extragalactic targets. One region of sky, situated near Baade's Window, contains most of the patches we have identified. Our optimal field, centered at RA:  $7^{\text{h}}24^{\text{m}}3^{\text{s}}$ , Dec:  $-1^{\circ}27'15''$ , has an additional advantage of being accessible from both hemispheres. We propose a figure of merit for quantifying real-world adaptive optics performance, and use this to analyze the performance of multi-conjugate adaptive optics in these fields. We also compare our results to those that would be obtained in existing deep fields. In some cases adaptive optics observations undertaken in the fields given in this paper would be orders of magnitude more efficient than equivalent observations undertaken in existing deep fields.

*Subject headings:* Astronomical Techniques, Astronomical Instrumentation, Astrophysical Data, Galaxies

---

<sup>1</sup>Department of Astronomy & Astrophysics, University of Toronto, 50 St. George Street, Toronto, ON, M5S 3H4 Canada

<sup>2</sup>Centre for Astrophysics and Supercomputing, Swinburne University of Technology, 1 Alfred St, Hawthorn, Victoria 3122, Australia

<sup>3</sup>Research School of Astronomy and Astrophysics, Institute of Advanced Studies, The Australian National University, Canberra A.C.T., Australia

<sup>4</sup>Gemini Observatory, Southern Operations Center, c/o AURA, Casilla 603, La Serena, Chile

<sup>5</sup>Observatories of the Carnegie Institution of Washington, 813 Santa Barbara Street, Pasadena, CA 91101

<sup>6</sup>Sterrewacht Leiden, P.O. Box 9513 NL-2300 RA Leiden, The Netherlands

<sup>7</sup>Centro de Astrofísica, Universidade do Porto, Rua das Estrelas, 4150-762 Porto, Portugal

<sup>8</sup>Canada-France-Hawaii Telescope Corporation, 65-1238 Mamalahoa Highway, Kamuela, Hawaii 96743, USA

<sup>9</sup>Institut d'Astrophysique de Paris, UMR7095 CNRS, Université Pierre et Marie Curie, 98 bis Boulevard Arago, 75014 Paris, France

<sup>10</sup>The United States Naval Observatory, 3450 Mas-

## 1. Introduction

Our understanding of the high-redshift universe has been revolutionized by deep fields, several of which have been extensively surveyed at all accessible wavelengths. Figure 1 shows an up-to-date summary of the locations of all existing deep fields (red circles). These fields have been primarily used to study galaxy formation and evolution out to very high redshifts (Cowie et al. 1995; Yee et al. 2000; Labbé et al. 2003; Bell et al. 2004; Egami et al. 2004; van Dokkum et al. 2004; Arnouts et al. 2007; Davis et al. 2007; Scoville et al. 2007; Bouwens et al. 2010; Ono et al. 2010). Because galaxies at such high redshifts are typically  $< 1\ \text{arcsec}$  in size, kinematical investigations of galaxies in these fields require adaptive optics (AO) spectroscopy (Law et al. 2009; Förster-Schreiber et al. 2009). The promise of

---

sachusetts Ave, NW, Washington, DC 20392-5420

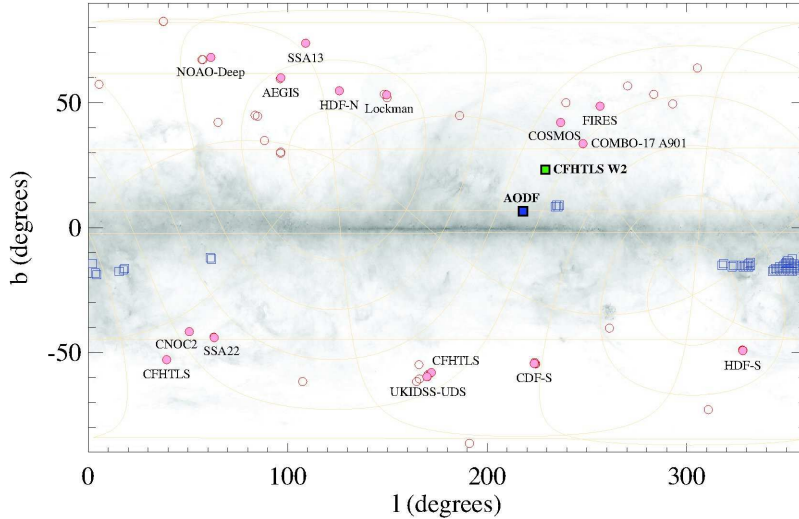


Fig. 1.— The galactocentric coordinates of existing deep fields (red circles) and the locations of the fields better suited for AO observations presented in Table 1 of this paper (blue squares, see Section 3 for details). The location of the fields has been overplotted on the dust emission map from the Schlegel, Finkbeiner & Davis (1998) study. Labeled existing deep fields are indicated with filled circles. The green square denotes a 1 square degree region within the CFHTLS W2 field (Section 5.2). The field labeled ‘AODF’ is our suggested optimal field whose properties are studied in detail in Sections 4 and 5.

such observations has been held out as an exciting next step for over a decade (e.g., Ellis et al. 1997). Unfortunately, it is now clear that only very limited AO observations are going to be undertaken in any existing deep fields.

Coupling integral-field spectroscopy to AO is crucial for understanding the formation of massive galaxies, particularly disks, since at high-redshift it has proven difficult for slit spectroscopy to reliably identify kinematic disks as kinematic and morphological axes are not necessarily correlated (Erb et al. 2006). Even at intermediate redshift ( $z \sim 0.6$ ), it has been demonstrated that galaxies are already kinematically complex and that 3D integral field spectroscopy (IFS) is essential to physical understanding and kinematic modeling (Rix et al 1997; Flores et al. 2006). At the highest redshifts AO IFS observations by some groups have given different results compared to non-AO observations of other groups. For example Laser Guide Star (LGS) AO observations with kpc resolution (Law et al. 2009) show that  $z = 2 - 3$  Lyman-break selected galaxies have high intrinsic velocity dispersions and no significant

rotational gradients about a preferred kinematic axis (Law et al. 2009). Förster-Schreiber et al. (2009) found similarly high velocity dispersions but a much greater incidence of disk rotation in a predominantly non-AO dataset of predominantly near-IR selected galaxies. It remains inconclusive whether such differences arise from a difference in sample (massive vs low mass galaxies) or the fact that the non-AO data has seven times poorer resolution on average in natural seeing. This is an important question: physical differences in kinematics at high-redshift may diagnose the prevalence of fast gas accretion along cold flows in the early Universe (e.g., Bournaud et al. 2007), but they may also arise from sample selection effects or observational limitations (for example Green et al. (2010) suggest it is simply the high-star-formation rates which drive the large velocity dispersions). Most IFS observations at high-redshift are still done without AO due to the technical difficulties of AO and also to the practical difficulties of finding enough targets near sufficiently bright stars in existing deep field samples.

The next stage in the development of this field

is to complement kinematical studies by probing chemical abundance gradients at a sub-kpc scale in star-forming galaxies, and to extend existing kinematical investigations to encompass more representative galaxies. This requires AO systems to be operating more efficiently (i.e. without performance limitation imposed by natural guide-star availability) and, ultimately, to multiplex if truly large samples are to be obtained. A step in this direction is already being taken with the MASSIV survey on the VLT, which targets star-forming galaxies in the redshift range  $1 < z < 2$  with SINFONI (Epinat et al. 2009; Queyrel et al. 2009). The targets are more representative than those being probed by SINS, with median stellar masses of  $\sim 10^{10} M_{\odot}$  and median star formation rates of  $\sim 10 M_{\odot} \text{yr}^{-1}$  (the corresponding values for SINS are  $\sim 10^{10.5} M_{\odot}$  and  $\sim 30 M_{\odot} \text{yr}^{-1}$ , respectively). However, most of the SINFONI data acquired during the MASSIV survey are seeing-limited leading to a final median spatial resolution of  $\sim 0.6\text{--}0.7''$  with only 25% of the MASSIV sample presently being observed with adaptive optics. Of these AO targets only a few are being acquired with the smallest pixel size ( $0.05''$ ). The main reasons are (i) the limitations in the availability of natural guide stars which precludes usefully observing at finer available pixel scale, and (ii) the difficulty to reach the depth required to probe the low-surface brightness component of galaxies in a reasonable exposure time with the smallest pixel size. This latter point leads to expectations of considerable progress in this subject with the advent of 30m-class Extremely Large Telescopes (ELTs).

A basic problem with undertaking AO in existing deep fields, even with laser guide stars, is that one still needs at least one reasonably proximate natural guide star to supply the information needed for tip-tilt correction (Rigaut & Gendron 1992). In contrast, two of the main selection criteria when identifying deep fields have been that they contain as few bright stars as possible to avoid light scattering contamination and saturation in long exposures, and that they lie in regions of low Galactic extinction (e.g., Alcalá et al. 2004). Thus all existing deep fields are near the Galactic poles, where the density of suitable natural guide stars is near a minimum. For example, Davies et al. (2008) report that only 1% of the Lyman break galaxy sample of Mannucci

(2007) are accessible to the VLT laser guide star system (Bonaccini et al. 1999): the loss of 75% of the targets is due to the absence of suitably close natural guiding stars (NGS), while additional 25% are lost after suitable color cuts and elimination of systems at redshifts obscured by strong OH features. The situation is similar with Gemini, whose AO system has similar sky coverage (Ellerbroek & Tyler 1998). Even with the upcoming Gemini Multi-Conjugate AO system (MCAO), the  $H$ -band sky coverage at the galactic poles will only be around 15% (Rigaut et al. 2000), and large benefits for MCAO emerge from having more than the minimum number of natural guide stars. This is because the geometry of the guide stars on the sky impacts the uniformity of Strehl ratio (Flicker & Rigaut 2001).

The issue of guide star rarity in deep fields becomes prominent in cases where target source density is low. This is often the case for extragalactic programs which focus on unusual objects. For example, many of the key projects described in the JWST Design Reference Mission (Gardner et al. 2006) rely on either extreme depth or serendipitous lines-of-sight. If such JWST observations are to be synergistic with ground-based AO follow-up, in particular with next generation telescopes like TMT or E-ELT, they cannot be undertaken efficiently in any existing deep field. It would be disappointing indeed if only 1%–10% of rare targets imaged with JWST in a deep field could be followed-up with a ground-based integral field units (IFU). It is becoming clear that existing and planned AO systems are set to enable transformative high-redshift science, but they will do so only in the regions of the sky in which they are effective. It is arguable that no existing deep field is suitable for efficient extragalactic AO work (though of course the cost of obtaining ancillary data equivalent to that already obtained in existing deep fields may overwhelm the gains obtained from high-efficiency adaptive optics).

In this paper we report on the results we have obtained in searching for those fields on the sky most suitable for high-efficiency extragalactic adaptive optics observations. In Section 2 we describe the important characteristics of deep fields in the context of adaptive optics observations, such as the acceptable level of dust extinction, field size, and magnitude range of natural guide

stars. In Section 3 we describe our attempts to identify the most suitable areas on the sky for undertaking extragalactic AO work, which is based on the strategy of combining information from all-sky stellar density and extinction maps. Our preferred ‘AO-friendly’ field and its first imaging results are described in Section 4. In the following Section 5 we define a figure of merit for adaptive optics and use this to compare the efficiency of AO observing in the proposed fields relative to the efficiency in representative deep fields. Our conclusions are summarized in Section 6. All magnitudes in this paper are based on the Vega system.

## 2. Desirable characteristics of extragalactic fields optimized for adaptive optics

In this section we consider the desirable characteristics of extragalactic fields optimized for adaptive optics. The relevant considerations include the maximum acceptable level of extinction from the intergalactic medium, the minimum useful area on the sky, and number density and magnitude range of available natural guide stars. We will consider each of these factors in turn, and discuss the importance of each of these factors using very general principles, in order to look for considerations that will remain relevant for future AO systems.

### 2.1. Extinction

Although most adaptive optics is undertaken in the near-infrared where extinction is lower than at visible wavelengths, it is clear that for any number of reasons, including reliability of photometric redshifts and ‘future-proofing’ the fields so as to make them useful when AO work moves to shorter wavelengths, that the ideal fields will lie in regions of low Galactic extinction. As any glance at the night sky will attest, patchy extinction can be rather high in regions with high star counts. It is therefore important to define an upper limit to the acceptable extinction in order to exclude unsuitable fields. A value of  $E(B - V) \sim 0.15$  mag is a good starting point, because Fukugita et al. (2004) and Yasuda et al. (2007) show that galactic extinction estimates become fairly unreliable in regions with  $E(B - V) \gtrsim 0.15$  mag. To err on the conservative side, in this paper we will use an upper limit of  $E(B - V) = 0.1$  mag on the

mean extinction as a constraint when exploring star count surface density maps for suitable fields. We note that  $E(B - V) = 0.1$  mag corresponds to  $A_V = R_V \times E(B - V) \sim 0.3$  mag at visible wavelengths, and that this is a factor of three to ten times higher than the corresponding extinction in near-infrared (NIR) passbands used by current AO systems.

### 2.2. Field size

The next factor to consider is the required size of the field. For extragalactic fields, the area of the field is driven by a desire to minimize the impact of cosmic variance, because scale-dependent inhomogeneity is often the dominant source of error in measurements derived from galaxy populations within a survey volume. The survey volume naturally depends on the area on the sky and the chosen redshift range, but for concreteness we will assume that most extragalactic work will explore a range of redshifts from  $z = 0$  to  $z = 4$ , which encompasses most of the star-formation history of the Universe. For such surveys, areas on the order of a square degree are needed in order to maintain fractional errors on number counts near the 10% level, and to probe a wide range of cosmic structures. This is fairly easy to demonstrate using online tools such as the Cosmic Variance Calculator<sup>1</sup> described in Trenti & Stiavelli (2008), but an even simpler way to show this is to use the analytic expressions provided by Driver & Robotham (2010) to estimate and compare cosmic variance for different field sizes. These authors employed counts of galaxies near the characteristic break in the luminosity function ( $M^*$ ) in the Sloan Digital Sky Survey Data Release 7 (SDSS DR7, Abazajian et al. 2009) to derive an empirical expression connecting cosmic variance and survey volume. Assuming a single sight-line and a rectangular geometry, the fractional error in the counts of  $M^*$  galaxies is given by:

$$\begin{aligned} \zeta &= (1 - 0.03(\sqrt{(A/B) - 1}) \\ &\quad \times (219.7 - 52.4(\log_{10} [A \cdot B \cdot 291.0]) \\ &\quad + 3.21(\log_{10} [A \cdot B \cdot 291.0]^2)) \\ &\quad \sqrt{C/291.0}. \end{aligned} \tag{1}$$

<sup>1</sup> <http://casa.colorado.edu/~trenti/CosmicVariance.html>

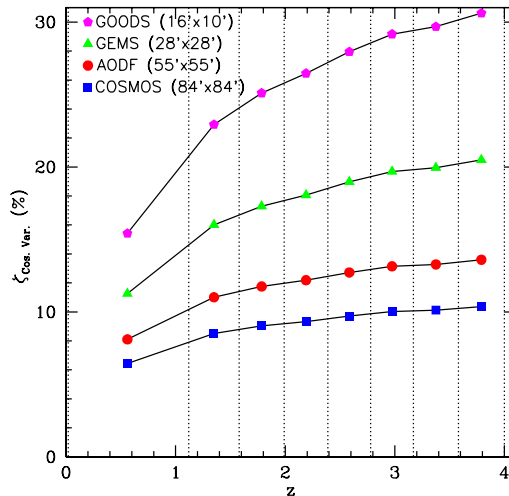


Fig. 2.— Cosmic variance, quantified using Eq. 1, as a function of redshift for four fields covering different areas on the sky. Redshifts of presented points correspond to median values for redshift ranges indicated with dotted lines. The effect of small-scale inhomogeneity on the field size we propose ( $\sim 1$  square degree, denoted as AODF) is comparable to the COSMOS field cosmic variance, and much less prominent than in the other two (smaller) fields, GEMS and GOODS.

where  $A$ ,  $B$ , and  $C$  are the median redshift transverse lengths and the radial depth of the survey, respectively, expressed in units of  $h_{0.7}^{-1}$  Mpc. (Note that the derived cosmic variance is for  $M^* \pm 1$  mag population only and will take higher values for more massive halos, see e.g., Moustakas & Somerville 2002). Results computed using this equation are presented in Figure 2, which shows the calculated cosmic variance for a number of surveys, and compares these with our proposed field size of around one square degree (actually  $55' \times 55'$ , for technical reasons described below).

Figure 2 shows that the calculated cosmic variance for our proposed field size results in fractional counting errors of around 10 – 15% (per unit redshift interval) for counts of  $M^*$  galaxies at redshifts between  $z = 1$  and  $z = 4$ . This is only slightly higher than for the COSMOS field (Scoville et al. 2007), but quite significantly better than for smaller volume survey fields, such as GEMS (Rix et al. 2004) and GOODS (Dickinson et al. 2003). On this basis alone we would argue that something around square degree is probably the right minimum size

for a contiguous area survey field intended to allow a broad range of investigations using adaptive optics, although another important factor is that a survey of this size will contain many thousands of strong line emitting objects, which are obvious targets for present-generation AO systems.

We have computed the surface density of strong  $H_\alpha$  line emitters (which we define to be  $F_{H_\alpha} > 10^{-16}$  erg cm $^2$  s $^{-1}$ , corresponding to the flux density of bright line emitters in Förster-Schreiber et al. 2009; Law et al. 2009) on the basis of direct measurement (Villar et al. 2008; Shim et al. 2009) as well as using indirect estimates scaled from UV flux (Bouwens et al. 2009) and measurements of [OII] (Cooper et al. 2008). By incorporating all the available information we estimate this value to be 2–5  $H_\alpha$  line emitters with flux  $> 10^{-16}$  erg cm $^2$  s $^{-1}$  Å $^{-1}$  per square arcmin at  $1 < z < 1.5$ , declining to 1–2 per square arcmin in the redshift interval  $2 < z < 2.5$ . The deep fields proposed in this paper will thus have around 10,000 suitable targets for AO-based follow-up. A significant fraction of these will be lost for various reasons (e.g., if  $H_\alpha$  lies on an airglow emission line, Davies et al. 2008), and a small number of

remaining objects will still lack suitable guiding stars (see Section 5). However, thousands of AO-accessible targets will remain, presenting a multiple order-of-magnitude change from the current situation.

### 2.3. Guide star limitations

We now explore the brightness of natural guide stars needed for effective use of adaptive optics. Our focus will be on the the following three classes of AO systems:

- Case 1: Laser-assisted adaptive optics systems on 8m-class telescopes, for which natural guide stars are needed to supply tip-tilt corrections. Such systems will define the state of the art for the next few years.
- Case 2: Ground-layer adaptive optics systems for 4m-class telescopes. Such systems are now being proposed as a means of revitalizing 4m-class facilities (e.g CFHT 'IMAKA, Lai et al. 2008). These facilities will also require natural guide stars for tip-tilt correction.
- Case 3: AO systems on 30m-class telescopes, some designs for which rely on AO for routine operation. In this case we mainly seek fields with an abundance of natural guide stars bright enough to feed laser-*unassisted* AO systems. Laser beacons may not be available at all times, and the existence of extragalactic fields in which they are not essential may be extremely attractive for telescopes that heavily emphasize AO.

We will begin by first outlining the general problem before focusing on the parameter space appropriate to the specific cases above. As will be shown below, in practise it is Cases 2 and 3 that drive our chosen magnitude limits.

In order to function an AO system needs to capture photons from a star, compute a correction, and apply this correction to an optical surface. The frequency over which an AO system must operate is set by the velocity of the atmosphere and the atmospheric coherence length. The coherence length is the length scale over which the index of refraction of the atmosphere is effectively constant, and is typically around 10 cm at a good

site. Wind speeds in the upper atmosphere are around 20 m/s, so it typically takes around 0.005s for a patch of atmosphere to move a coherence length (Rogemann & Welsh 1996). The minimum frequency of an AO system is therefore around 200 Hz, although in reality one would want to both Nyquist sample the signal and allow time for actuator lag in applying a correction, so a realistic minimum is around 1 kHz.

How many photons from a natural guide star are needed in this time depends on the specific type of correction, but we can bracket our analysis by considering two extremes: (i) tip-tilt correction, for which relatively faint stars suffice, and (ii) full correction to obtain diffraction-limited performance, for which bright stars are needed.

A zeroth magnitude star has a  $R$ -band flux of 3080 Jy at the top of the atmosphere<sup>2</sup>, corresponding to  $2.02 \times 10^{11}$  photon/m<sup>2</sup>/s (Bessell 1979). Thus an 8m telescope captures  $\sim 600$   $R$ -band photons from an 18th magnitude star in one millisecond. In the foreseeable future no AO system will have a quantum efficiency approaching unity, but even with an end-to-end efficiency of 20% over 100 photons will remain, which is ample for obtaining a reasonable centroid. Thus, at least in principle, an AO system on an 8m telescope can use  $R = 18$  mag stars for tip-tilt corrections. Since the number of photons from a star imaged with a 30m telescope is about fourteen times greater than for an 8m telescope, a 30m telescope can do tip-tilt corrections on guide stars down to around  $R = 21$  mag. On the other hand, a 4m telescope needs stars of about  $R = 16.5$  mag for tip-tilt corrections. We emphasize that these numbers are all for rather idealized AO systems. For example, in the real-world situation of the Gemini Altair AO system, tip-tilt reference stars of around  $R \sim 16.5$  mag (over a magnitude brighter than the somewhat ideal case discussed above) are found to be highly desirable for high-performance AO operation.

Much brighter natural guide stars are needed for use with natural guide AO star systems that attempt to achieve diffraction-limited performance. In this case the size of relevance is not the full aper-

<sup>2</sup>For concreteness we consider the brightness of guide stars at visible wavelengths, though the argument can be generalized to stars at arbitrary wavelength.

ture of the telescope, but rather the sub-aperture defined by the coherence length of the atmosphere which in turn drives the number of needed actuators. An  $R = 13$  mag star supplies  $\sim 10$  photons in 1 ms to a 10 cm diameter sub-aperture. The number of photons per bin needed to reliably compute a wavefront depends critically on factors such as the read noise of the detector, but ten photons per coherence-length sized patch on the pupil is a reasonable lower limit. Note that in the case of diffraction-limited AO (and unlike the case with tip-tilt correction), having a larger telescope does not gain one a fainter magnitude limit for natural guide stars, and in fact AO becomes harder because the system requires more actuators. We also note that the presence of bright stars ( $R \lesssim 14$  mag) in the field *with* AO correction can potentially cause problem for infrared (IR) detectors by leaving long-lasting (up to an hour) residual flux. Although this would affect imaging in case when AO correction is applied across a wide field of view, the main motives for developing an AO-friendly deep field (see Sections 1 and 5) are high resolution IFU or multi-object spectroscopic surveys, that would not be influenced.

On the basis of the considerations just given, our search for locations on the sky suitable for extragalactic adaptive optics focuses on stars in the magnitude range  $13 < R < 16.5$  mag. The bright end is set by the apparent magnitude of stars needed to supply guide stars for natural guide-star AO systems (independent of telescope aperture), which is essentially Case 3 above. The faint end is set by the apparent magnitude of stars needed to supply tip-tilt reference stars for real-world operation of existing AO systems on 8m-class telescopes (Case 1) and for ideal-case laser-based ground-layer AO with 4m-class telescopes (Case 2 above).

### 3. Identification of the suitable fields for Adaptive Optics

In order to find the regions on the sky with the properties we have just described, we rely on full sky reprocessed composites of the COBE/DIRBE and IRAC/ISSA dust maps (Schlegel et al. 1998) and the UCAC2 astrometric catalog of  $\sim 5 \times 10^7$  stars with declination in the  $[-90 \text{ deg}, +(40 - 52) \text{ deg}]$  range (Zacharias et al. 2004). We constructed a full sky map of star count surface

density for UCAC2 stars in the range  $13 - 16.5$  mag using the HEALPIX data analysis package (Górski et al. 2005) that performs pixelization of the sphere with equal area pixels. Two maps have been produced: one with the resolution of  $6'.871$  to match the resolution of the available HEALPIX map of Galactic reddening  $E(B - V)$  and the other (see Figure 3) with the coarser sampling of  $55'$  (the HEALPIX resolution that is closest to the  $1^\circ \times 1^\circ$  field size, see Section 2.2). The resolution of the existing  $E(B - V)$  map was degraded to match the  $55'$  resolution of the star counts surface density map by taking the average extinction value for each cell. The coarse resolution extinction and star count maps are both shown as panels at the top-left and top-right of Fig. 3. Note that the UCAC2 catalog has a gap in coverage at high declination (shown in gray in the figure), but any AO-optimized fields which might exist at these very high declinations would be generally unsuitable anyway. Any such fields would be inaccessible from Chile and be at quite high airmass most of the time for major northern hemisphere observatories (including those on Mauna Kea).

Before proceeding with a detailed analysis, it is instructive to note that many positions in the sky likely to be suitable for our purposes can be identified easily by simply looking for maxima in a map obtained by multiplying the stellar density map by the inverse of the extinction map. This is shown as the large bottom panel in Figure 3. Local maxima in this map do not necessarily define regions suitable for AO, because some local maxima correspond to regions with low star counts but extremely low extinction. However, this figure acts as a natural starting point for the next step in our analysis.

Having identified candidate fields using the analysis just described, we then looked at all the candidate fields individually to try to better understand their characteristics. To be explicit, we first identified all HEALPIX cells whose  $13 < R < 16.5$  mag stellar density  $\Sigma_{\text{sc}}$  was  $\Sigma_{\text{sc}} > 0.5 \text{ arcmin}^{-2}$  and whose extinction was  $E(B - V) \leq 0.1$ . We found 442 one square degree cells met these criteria, and these were then examined further. The distribution of stellar density and extinction for these cells is shown in Fig. 4, color-coded by right ascension. In order to cull

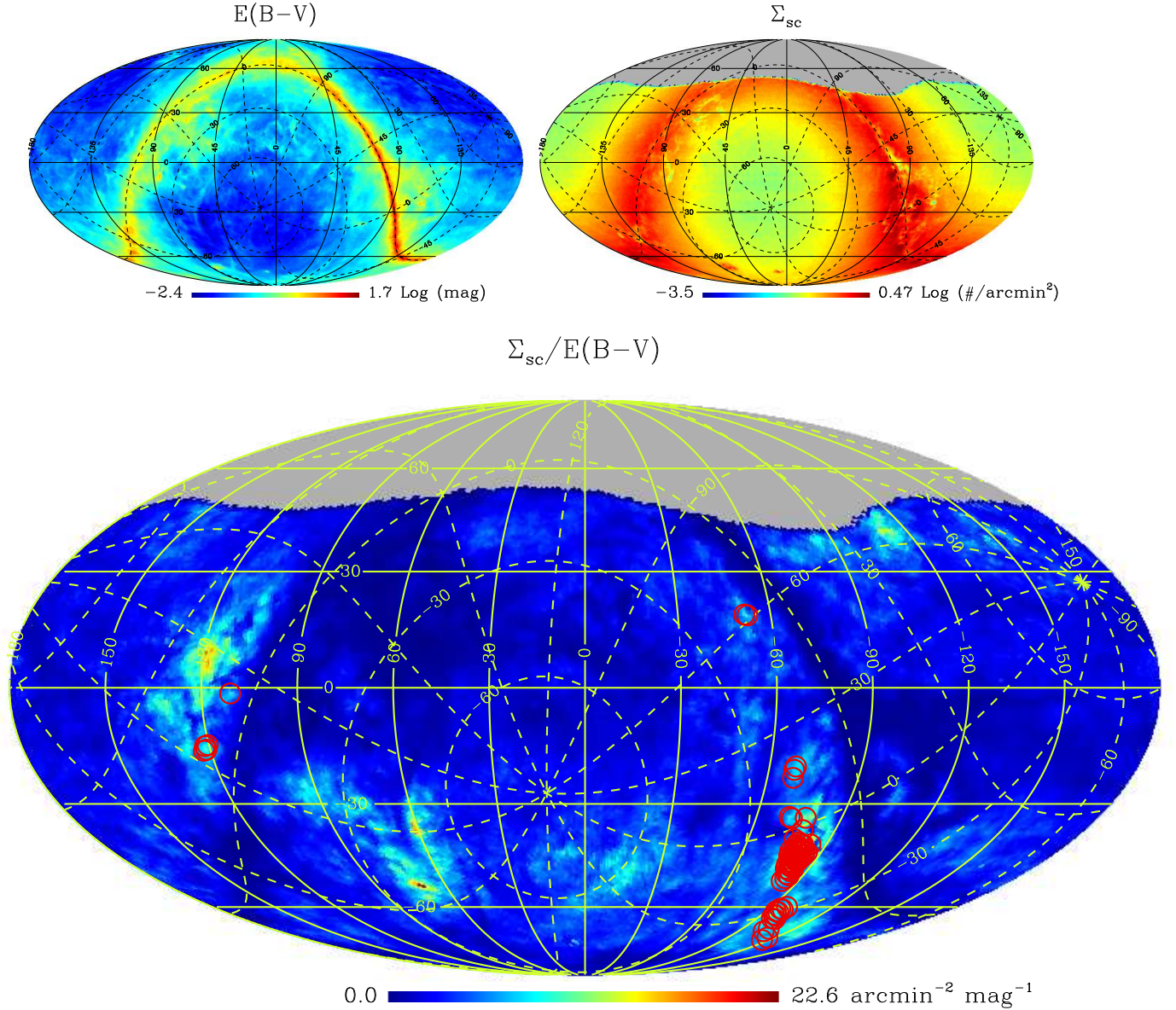


Fig. 3.— (*Top left:*) An all sky map of extinction, scaled logarithmically. The solid line grid corresponds to the celestial coordinate system with RA in degrees increasing to the left. Zero degrees lies at the center of the figure. A Galactic coordinate system is over-plotted with dashed lines. (*Top right:*) The corresponding map of star count surface density for stars in the 13 – 16.5 magnitude range. The region shown in gray corresponds to a high declination gap in coverage in the UCAC2 stellar catalog. As noted in the text, any AO-friendly fields which might exist at very high declination would be unsuitable for other reasons. (*Bottom:*) A map constructed by multiplying the map at the top left by the inverse of the map at the top right. Maxima in this figure correspond to potentially interesting locations for undertaking extragalactic adaptive optics observations. Red circles present the positions of 67 fields well-suited to extragalactic AO. See text for details.



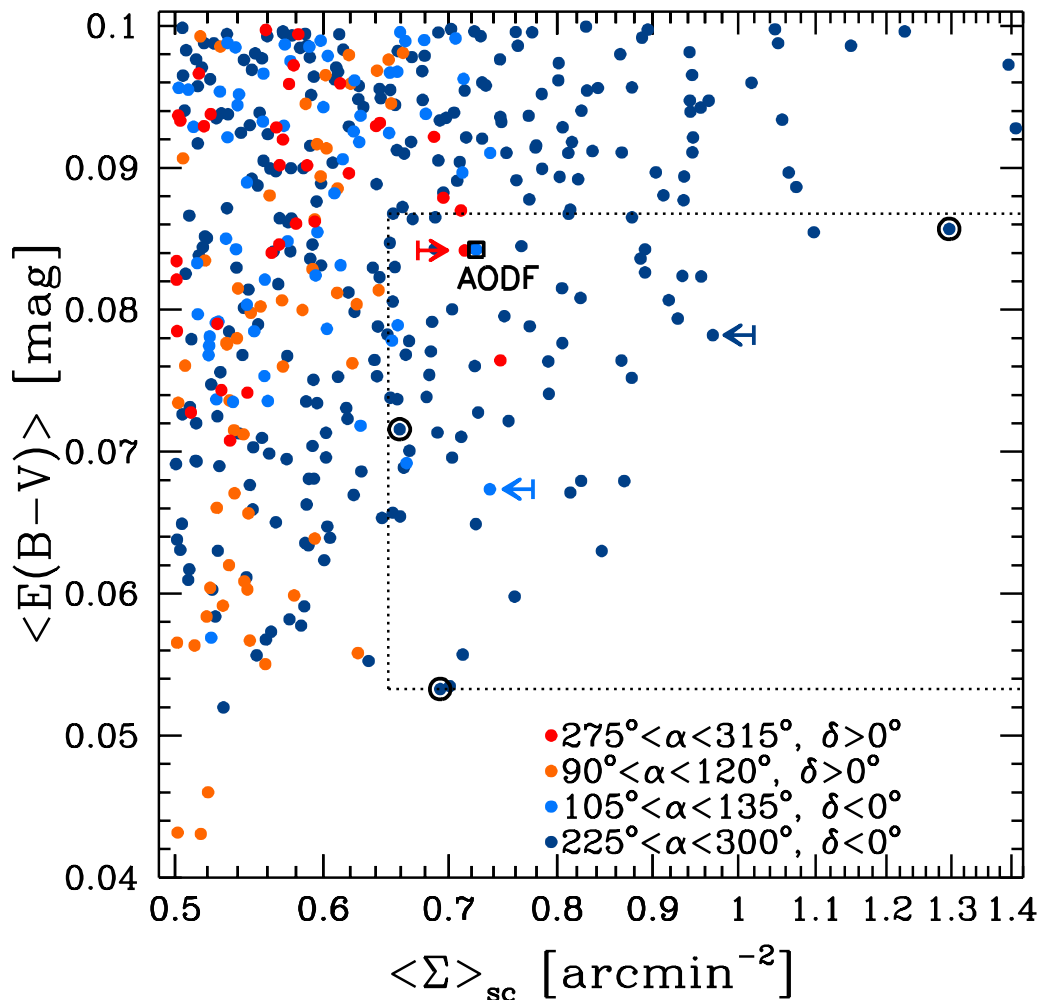


Fig. 4.— Extinction  $E(B-V)$  as a function of the star counts surface density  $\Sigma_{\text{sc}}$  for 442  $55' \times 55'$  fields with  $\Sigma_{\text{sc}} > 0.5 \text{ arcmin}^{-2}$  and  $E(B-V) \leq 0.1$ . The fields are color-coded based on their equatorial coordinates. The dashed line encloses 67 fields with  $\Sigma_{\text{sc}} \geq 0.65 \text{ arcmin}^{-2}$  and  $0.05 \lesssim E(B-V) [\text{mag}] \lesssim 0.087$ . The fields flagged with open circles have the highest star counts surface density or the lowest mean extinction or its standard deviation. Colored arrows point at the representative fields for each of the three sightlines (see Appendix A for details). The proposed ‘optimal’ field described in Section 4 is labeled ‘AODF’ and flagged with an open box.

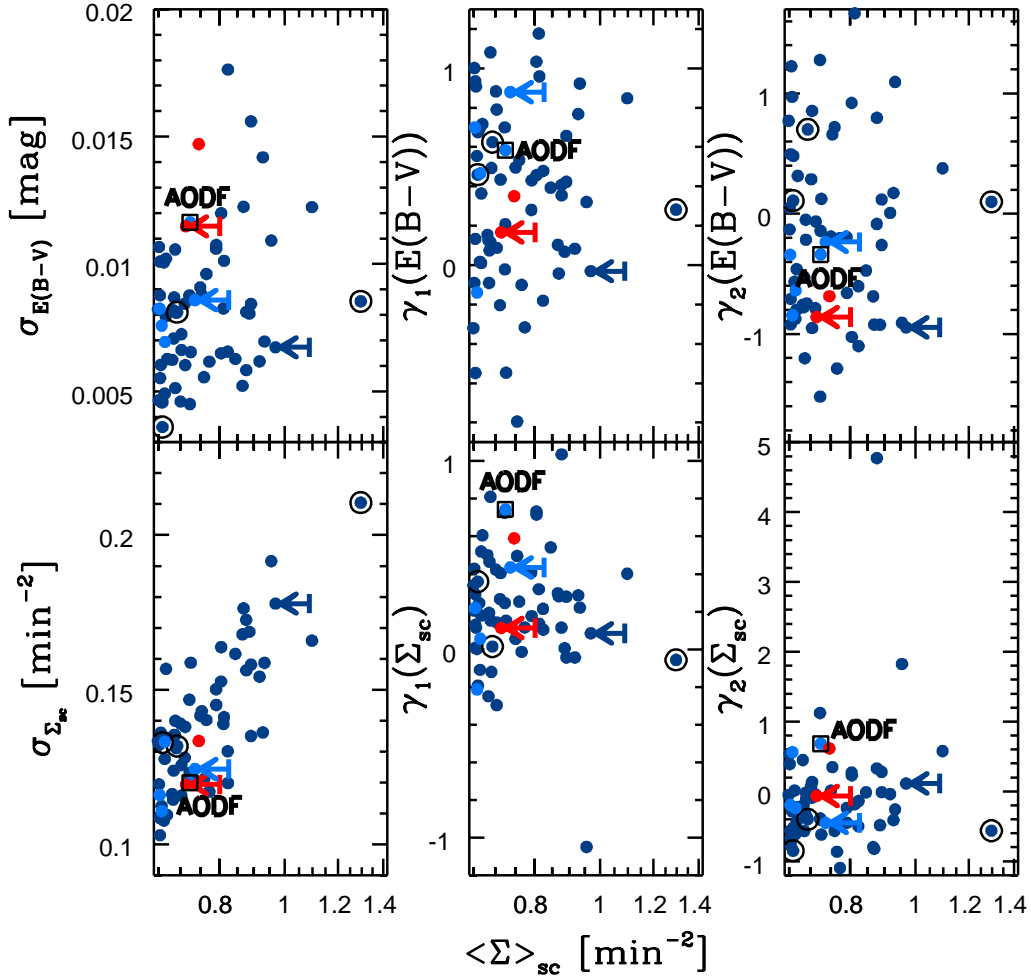


Fig. 5.— The three higher-order moments of the extinction and star count surface density distributions as functions of the mean star count surface density for 67 fields from Table 1. The fields are color-coded based on their equatorial coordinates, as given in Figure 4. The fields flagged with open circles or with colored arrows correspond to the flagged fields in Figure 4. Our optimal AO-friendly field is labeled as in Figure 4.

these fields down to a more manageable number, we then restricted the sample further to include only those fields whose extinction is lower than the average extinction, and whose stellar density is higher than the average density. This translates into selecting fields with a stellar density greater than  $0.65 \text{ arcmin}^{-2}$  and reddening less than  $\sim 0.087 \text{ mag}$ . This final cut corresponds to selecting fields inside the dashed region shown in Fig. 4, and brings the total number of fields down to 67 from 442. The positions of these fields are shown as solid dots in Figure 3 and blue squares in Figure 1.

The locations and properties of the 67 fields are given in Table 1. Variances and higher-order moments of stellar counts and extinction within each field are also tabulated. These moments are based on computations within sub-cells with widths of  $6/871$ . The fields flagged with open circles in Fig. 4 have the highest star count surface density or the lowest average value or standard deviation of the reddening coefficient, and rows corresponding to these fields are italicized in the table. Colored arrows point at some more representative fields for the three sightlines (see Appendix A for details). A graphical summary of all higher-order statistics is presented in Figure 5, from which it can be seen that there is a substantial variation in the distribution of both stars and extinction throughout the fields we have identified. While all the tabulated fields should be quite good for extragalactic adaptive optics work, the best field for a given purpose will depend upon the specific application (e.g. upon whether it is more important to maximize uniformity of star counts, or to minimize absolute extinction, or to minimize variation in extinction). The various trade-offs that need to be balanced in order to choose the best field for a given set of requirements are explored in Appendix A.

#### 4. CFHT imaging results for a proposed ‘optimal’ field

All fields labeled in Figure 1 and in the lower panel of Figure 3 have exceptional characteristics in terms of stellar surface density and/or extinction<sup>3</sup>. However, a practical factor that has not

<sup>3</sup>It is interesting to speculate on why these fields exist. While many of them lie in the vicinity of Badde’s window,

yet been considered is the position of the field for accessibility with a broad range of telescopes. An ideal field lies near zero degrees declination in order to be reachable from both hemispheres. With this consideration in mind, the most interesting region for further analysis proves to be the rather large  $30^\circ \times 60^\circ$  region centered at  $RA = 8^h$ ,  $DEC = 0^\circ$  (see the bottom map in Figure 3). To identify the best one square degree patch within this region, we tessellated the region into  $55' \times 55'$  cells and explored the distribution of star counts and  $E(B - V)$  on a cell-by-cell basis. After identifying a handful of promising cells, we then looked for both low absolute extinction and uniformity in extinction within individual cells. (Uniformity in extinction is desirable for accurate photometric redshifts). Figure 6 shows the intra-cell stellar surface density and the extinction map for the best  $55' \times 55'$  cell, which we refer to as the ‘Adaptive Optics Deep Field’ (AODF). The field lies at RA:  $7^h 24^m 3^s$ , Dec:  $-1^\circ 27' 15''$  and is labeled with ID 8328 in Table 1. It has a stellar surface density of more than two stars per  $2' \times 2'$  region over  $> 99\%$  of its area. In addition, for  $> 85\%$  of the field presented in Figure 6 extinction is  $E(B - V) \leq 0.1$  ( $A_V < 0.3$ ; NIR extinction at AO wavelengths will be far lower, see Section 2). Another important practical consideration is that the number of very bright stars (which scatter and raise the sky background) in this  $\sim 1$  square degree field is low: there are only a handful of stars brighter than 11th magnitude in the field.

Since this ‘AODF’ field seems highly interesting for future follow-up, Director’s Discretionary time on the Canada-France-Hawaii Telescope was used to explore its properties further (and to act as a sanity check on the analysis presented in this paper). A 10 min snapshot in g’ and z’ bands was acquired using CFHT’s MegaCam in March 2010 in order to evaluate the distribution and color of the brightest stars in the AODF (see Bertin et al. 2002 for the description of the TERAPIX software modules designed for processing MegaCam data). The upper panel of Figure 7 presents the  $\sim 1^\circ \times 1^\circ$

---

characterized by very low dust content, a smaller group of fields is found near the Galactic anti-center. One possibility, suggested to us by Sidney van den Bergh, is that these fields have high counts but low extinction because metallicity decreases with increasing Galactocentric distance. As a result the Galactic anti-center has a low dust to gas ratio.

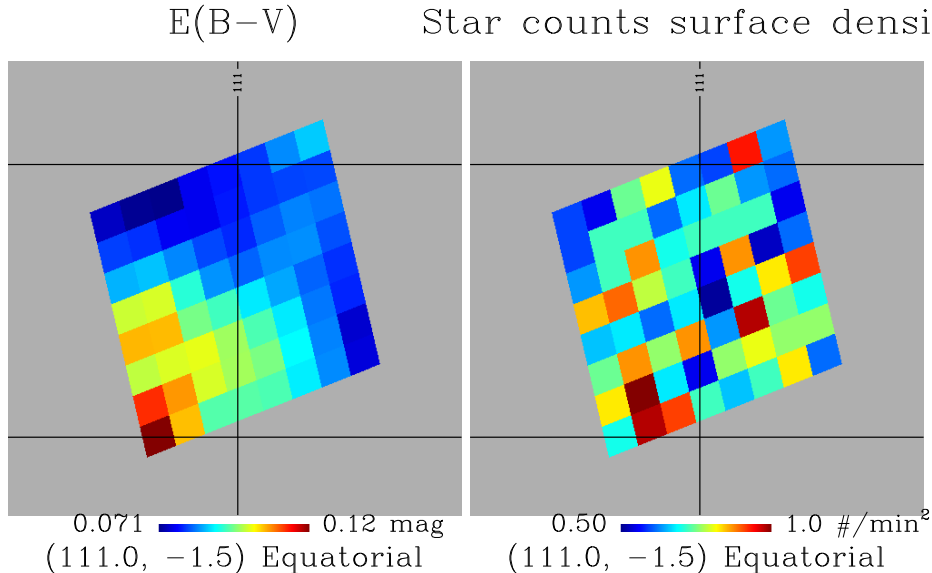


Fig. 6.— Extinction and star surface density maps centered on the position of our chosen field. Each pixel is  $6'.871 \times 6'.871$ . There are  $\gtrsim 2200$  13 – 16.5 mag stars suitable for AO guiding in the field corresponding to  $\sim 3300$  star-forming galaxy candidates with the number surface density of  $3 \text{ arcmin}^{-2}$ . The field is centered at  $RA = 7^{\text{h}}24^{\text{m}}2.67^{\text{s}}$ ,  $DEC = -1^{\circ}27'14.44''$ . Solid line grid corresponds to the celestial coordinate system with  $RA[^{\circ}] = 360^{\circ} - \alpha[^{\circ}]$

field of view (made out of 5 dithered exposures), and it is apparent here that bright stars are indeed sparse, with the most prominent one ( $V=9.9$  mag) in the center of the field. The main drawback of such a star is not the vertical blooming which affects a small fraction of the imaging area but the halos due to internal reflections in the MegaPrime optics: such a halo increases locally the sky background and limit detectivity. The upper panel of Figure 7 shows that there are four stars that cause a potential problem. Each halo covers a disk of  $3'$  in radius, leading to  $\sim 120$  square arcmin for the whole field. When compared to the MegaCam field of view of  $\sim 1$  square degree, those four halos produce a negligible loss of less than 4%. (We note that brighter galaxies can still be extracted from these areas).

We also compared AODF galaxy counts in  $g'$  and  $z'$  bands with the expected number based on the CFHT Legacy Survey (CFHTLS) Deep data (details on galaxy/star separation method used by the TERAPIX pipeline are given in Coupon et al. 2009). The resulting depth found in both  $g'$  and  $z'$  bands follow the expectations (within the range

of error), and the recovered galaxy number surface density closely tracks the distribution of CFHTLS Deep objects, as shown in the lower panel of Figure 7. The slight excess at the bright end is the combined effect of shot noise and cosmic variance (see Section 2.2), and the turnover at  $g = 24.5$  mag is due to the (much) shorter exposure time compared to the CFHTLS Deep.

We conclude from analysis of the CFHT data that all the characteristics discussed in this section (namely a position that allows observations from different sites, a large number of suitable tip-tilt stars for laser AO, a generally low and fairly uniform Galactic extinction, coupled with the small number of very bright stars) make this particular field an excellent choice for future deep extragalactic AO observations.

## 5. Real-world benefits of undertaking observations in AO-optimized fields

How do the properties of the fields identified in the previous sections compare with those of existing extragalactic deep fields? Figure 8 presents a

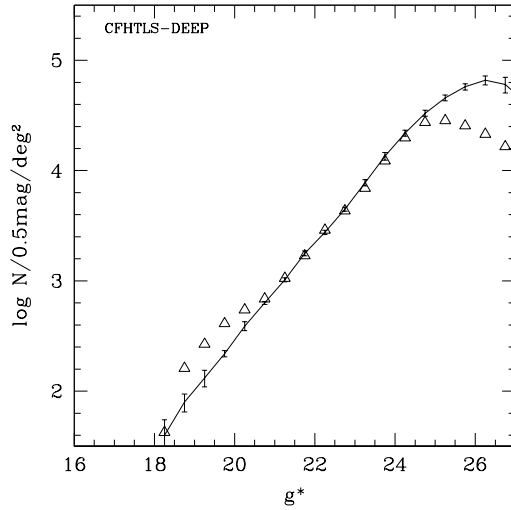
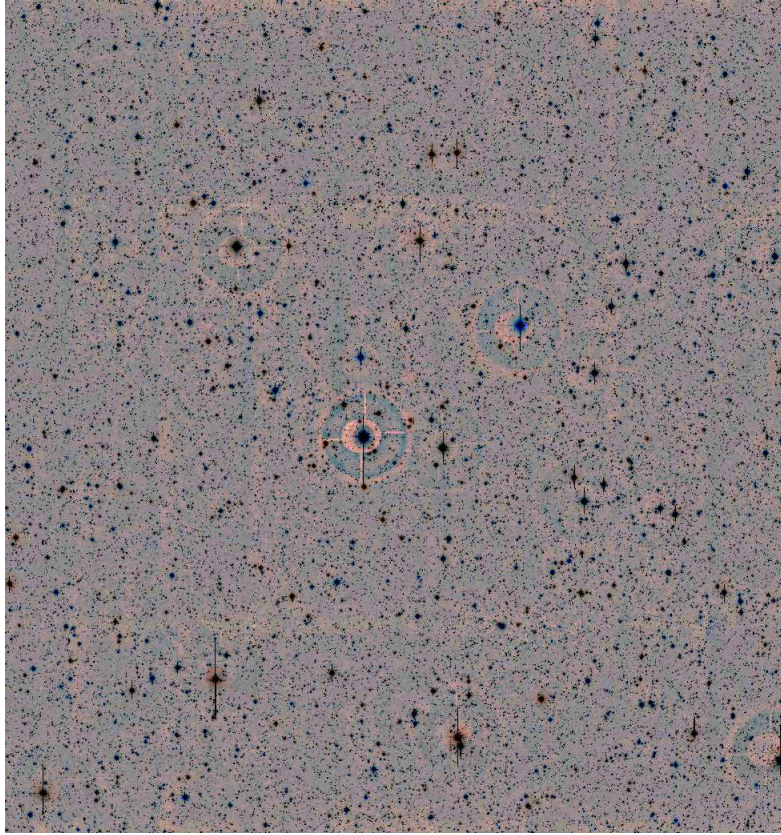


Fig. 7.— *Upper panel*: CFHT MegaCam  $g'$  and  $z'$  band mosaic of the  $1^\circ \times 1^\circ$  field centered on  $RA = 7^{\text{h}}24^{\text{m}}$ ,  $DEC = -1^\circ 27' 15''$ . Note that there are only a few bright stars in this field, with the brightest one (in the middle of the field) at  $V=9.9$  mag. *Lower panel*: Galaxy number per 0.5 mag and per  $1^\circ \times 1^\circ$  as a function of  $g'$  magnitude. Solid line represents the expected values based on CFHTLS Deep data set and triangles correspond to the recovered galaxy number counts.

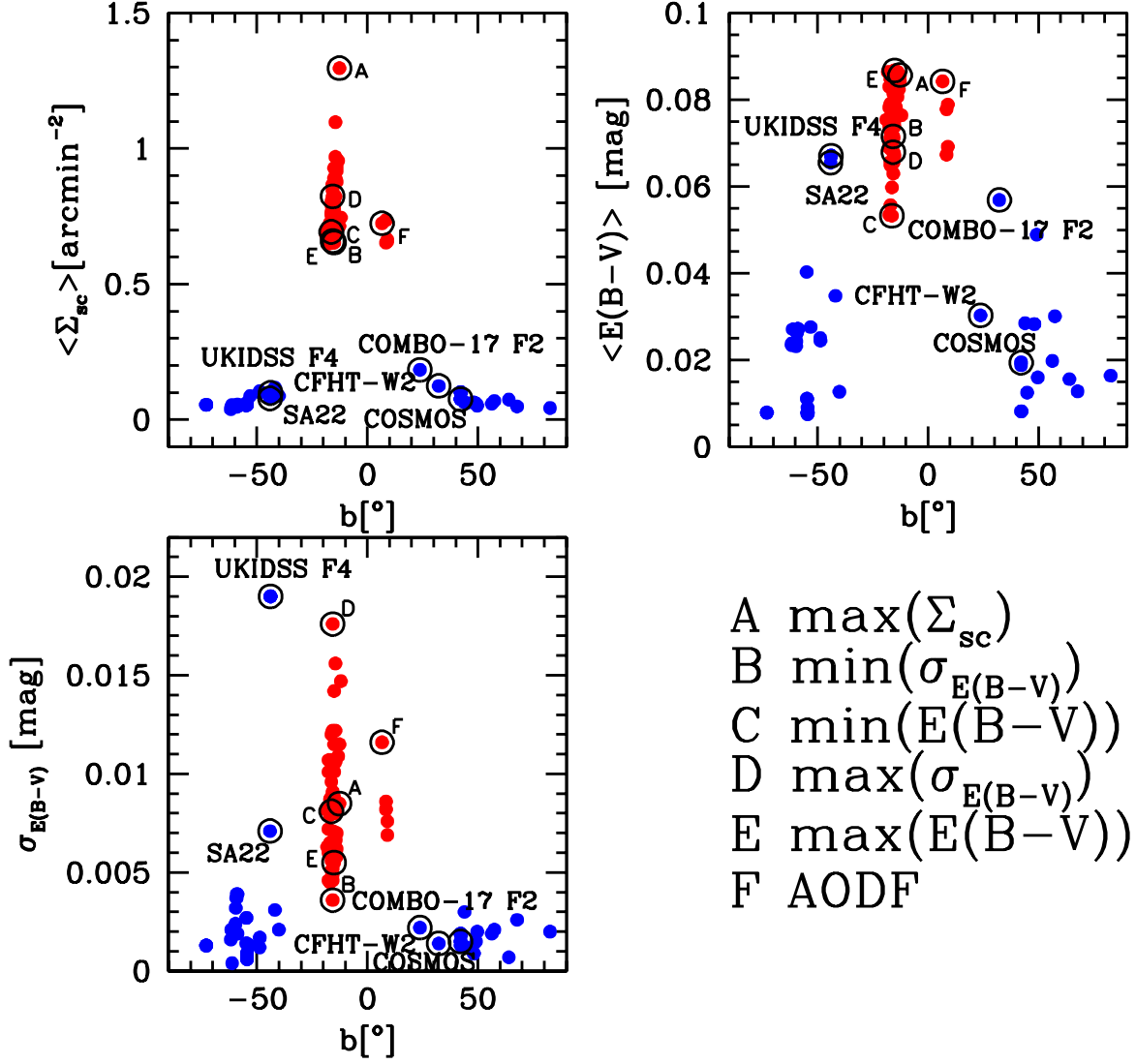


Fig. 8.— *Top left*: Stellar surface density as a function of Galactic latitude for two sets of deep fields: 55 existing deep fields plus 1 square degree region within the CFHTLS W2 field (blue filled circles) and 67 low latitude pointings we have explored in detail (red filled circles, detailed properties listed in Table 1). *Top right*: Average  $E(B - V)$  as a function of Galactic latitude for the same two sets of fields. *Bottom right*: Standard deviation of  $E(B - V)$  for the data in the other panels (this panel quantifies the patchiness of the extinction). Our chosen field (AODF) and five other fields from Table 1 with extreme properties are labelled.

comparison of the average stellar density, average extinction, and standard deviation of the extinction coefficient for the set of 67  $55' \times 55'$  fields from Table 1 to those in 55 existing deep fields<sup>4</sup>. Quantities are shown as functions of Galactic latitude, with our candidate fields shown in red, and existing deep fields in blue. Our preferred field is labelled ‘F’ in each panel. The figure illustrates that our proposed fields typically have over ten times the stellar density of existing deep fields coupled with extinction values and extinction variations across the field at the high end of those in existing deep fields<sup>5</sup>. How does this translate into practical performance benefits for undertaking AO observations? Are the existing fields already good enough? In order to investigate these questions, we will define a fairly generic figure of merit for AO observations in Section 5.1, and compare the distribution of this figure of merit in our proposed fields to the corresponding distribution in a typical existing deep field (Section 5.2).

For the sake of concreteness, much of the following analysis will be undertaken in the context of the predicted performance of the soon-to-be-commissioned Gemini Multi-Conjugate Adaptive Optics System (GeMS, Ellerbroek et al. 2003). GeMS is intended to feed NIR instruments with a high Strehl ratio beam at relatively short wavelengths (Strehl ratios up to  $\sim 50\%$  in  $J$ -band), and in particular to feed the FLAMINGOS-2 NIR MOS spectrograph (Eikenberry et al. 2004) and the GSAOI imaging camera (McGregor et al. 2004). The benefits of undertaking observations in the AODF are fairly obvious for science programs which use imaging cameras or resolved integral field spectrographs, but the AODF will also be of considerable interest for programs of NIR MOS spectroscopy. Some spatially resolved kinematical and chemical composition information can be recovered with narrow slits if these span individual objects that are not obliterated by seeing. Fur-

<sup>4</sup>From the list compiled by J. Brinchmann, see <http://www.strw.leidenuniv.nl/~jarle/Surveys/DeepFields/index.html>

<sup>5</sup>Note that in Figure 8 we have also included a region within the Canada-France Hawaii Survey Legacy Survey Wide-2 Field (CFHTLS W2). This is not technically a ‘deep field’, but CFHTLS W2 is worthy of inclusion because it is the most commonly-observed extragalactic field that lies in the general vicinity of our preferred field (for detailed descriptions and comparisons with this field, see Section 5.2).

thermore, AO-assisted MOS spectrographs will be able to effectively use narrow slits, which minimize background contamination.

We have chosen to focus our analysis on GeMS because it is the most advanced AO system likely to be available on 8m-class telescopes for the foreseeable future, and because Multi-Conjugate Adaptive Optics (MCAO) is virtually certain to be an important operational mode for future 30m-class Extremely Large Telescopes. We will not describe the fundamentals of MCAO here, and refer the reader to Rigaut et al. (2000) for an explanation of the general principles. For our purposes it suffices to note that MCAO’s purpose is to deliver high image quality over a wider area than conventional adaptive optics systems, and it does so by using a constellation of laser guide stars beacons and several natural guide stars to determine the shape of the wavefront, which is then corrected by multiple deformable mirrors. (The natural guide stars are essential, because they are needed in order to establish tip-tilt corrections). In the case of the GeMS MCAO system, five artificial guide star beacons and three natural guide stars are used. Another important point that should be emphasized here is that the precision of the tip-tilt corrections depends on distance from the guide stars, so the geometric arrangement of the natural guide stars plays an important role in establishing AO performance (Flicker & Rigaut 2001). We assume nominal performance of GeMS, and emphasize that both the areal coverage and PSF stability expected from MCAO are substantially larger than in the case with conventional (single-laser, single wavefront sensor) AO.

### 5.1. Figure of merit

Any number of figures of merit can be devised for inter-comparing the performance of various AO systems, but in this paper we propose to use a figure of merit that captures the basic idea that real-world AO performance generally depends not only on image quality, but also on the variation of that image quality over the field of view. We therefore adopt the following figure of merit:

$$F = \frac{1}{\sigma_S^{0.25} \times (1 - \langle S \rangle)^{1.5}} \quad (2)$$

where  $\langle S \rangle$  is the average Strehl ratio achieved in the field of view, and  $\sigma_S$  is the RMS variation in

Strehl over the field of view. In the present paper our purpose is to understand the impact of tip-tilt stars, so we will be calculating Strehl ratios using simulation software that computes the distortion in the wavefront due to anisokinetism and assumes perfect correction for other aberrations in the wavefront. Our procedure for doing this will be described in the next section.

The distribution of  $F$  across the sky characterizes the performance of an AO system. The specific values of the exponents in our definition of  $F$  are chosen to weight the peak Strehl at the expense of some uniformity in the value of the Strehl ratio over the field of view. However, uniformity in Strehl is not completely de-emphasized, and a guide star configuration resulting in a generally high but strongly variable Strehl across the field of view will have a significantly lower value of  $F$ . None of main conclusions of this paper are strongly dependent on the specific values of the exponents used in Equation 2, as shown in Appendix B.

## 5.2. MCAO observations in existing and proposed fields

To investigate limitations in MCAO performance in various fields as a function of natural reference star magnitudes and configurations, we used the Gemini MCAO simulator (F. Rigaut, private communication) to compute the distribution of the figure of merit  $F$  for  $\sim 1000$  uniformly distributed pointings within several fields. As noted earlier, we wish to study the errors introduced into the corrected wavefront by a paucity of tip-tilt stars, so the Strehl ratio used in our analysis isolates the RMS contribution to the distorted wavefront introduced by anisokinetism. In other words, the simulation assumes that all other contributions to the wavefront degradation are negligible, so if the tip-tilt correction were perfect, the Strehl ratio would be unity. In practise of course errors other than anisokinetism will contribute to the wavefront<sup>6</sup>. However, the point is that our analysis allows us to study *the best performance possible from the AO system*, limited only by the number of natural tip-tilt reference stars.

<sup>6</sup>The interested reader is directed to Table 2 of this web page for a census of other contributions to the MCAO wavefront:  
<http://www.gemini.edu/sciops/instruments/mcao?q=node/10749>

Each simulated pointing was  $80'' \times 80''$  in size (appropriate to Gemini's GeMS). We analyzed performance in the AODF, and for comparison with performance in un-optimized deep fields, we also examined  $\sim 1000$  uniformly distributed positions in the COMBO 17 Field 2 deep field and in the 1 square degree region of the CFHTLS wide field (W2). COMBO 17 Field 2 (labeled as A 901 in Wolf et al. 2003) was chosen because it is the existing deep field with the highest star counts. We chose to include (a part of) the CFHTLS W2 field in this comparison because (a) it is located fairly close to the AODF, and (b) its star counts surface density is high. However, large portions of this  $7^\circ \times 7^\circ$  field are 'contaminated' with very bright stars<sup>7</sup>. In order to avoid those regions we performed our analysis in the  $1^\circ \times 1^\circ$  subfield within CFHTLS W2 centered on  $RA = 8^h42^m$ ,  $DEC = -1^\circ15'$ , which has few very bright stars but an abundance of stars in the range suitable for tip-tilt correction.

To determine the optimal set of guide stars in each pointing, we looked for the best set of three stars with magnitudes in the range  $13 < R < 16.5$  mag with distances between  $40''$  and  $60''$  from the field center (these distances are set by the patrol fields of pick-off mirrors in GeMS). As noted by Flicker & Rigaut (2001), the ideal geometry for these stars is an equilateral triangle, so we searched for three stars lying in the  $40'' - 60''$  annulus whose interior angles were within  $60^\circ \pm 20^\circ$  from each other. If we failed to find suitable stars we then relaxed our criterion that the guide stars approximate equilateral triangles and simply searched for three stars defining a triangle with any set of side lengths. Where multiple triangles existed we retained the one that gave the best value of  $F$ . When three stars in any geometry could not be found we calculated MCAO performance with available stars, either singly or in pairs. In cases where no stars in the suitable magnitude range were found in the vicinity of our pointing, the value of  $F$  was set to zero.

The results from our investigation are shown in Figure 9, which compares the distribution and cumulative distribution functions of  $F$  for the AODF, shown in blue, with the corresponding dis-

<sup>7</sup>See <http://legacy.astro.utoronto.ca/Fields/images/w2.html>



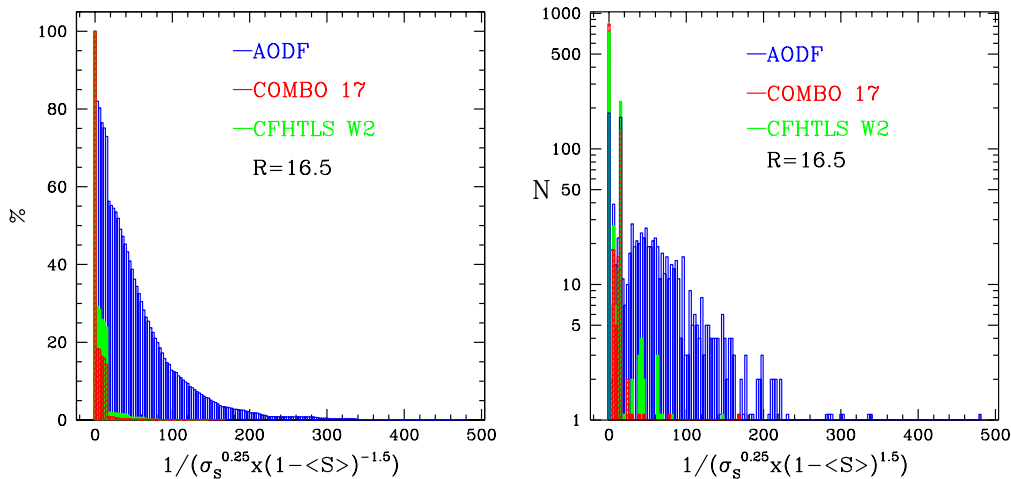


Fig. 9.— Cumulative distribution (*left*) and distribution (*right*) of our Strehl-related figure of merit for  $55' \times 55'$  AODF (blue), COMBO 17 Field 2 (red), and the CFHTLS W2 subfield (green). Data points are binned according to their figure of merit value in 3 unit wide bins. The left-side vertical axis gives the percentage of field area with the figure of merit value equal or higher than the corresponding bin’s lower limit. In the right-side panel ordinate represents the number of pointings contained in each bin. Both panels correspond to a guide star magnitude limit of 16.5 mag in  $R$ -band (foreseen bright time limit for the Gemini GeMS MCAO system). See text for details.

tributions for the COMBO 17 Field 2 and a 1 square degree region of the CFHTLS W2 field, shown in red and green, respectively. The two panels of Figure 9 correspond to a limiting natural guide star magnitude of 16.5 mag in  $R$ -band (corresponding to the anticipated limit for GeMS bright time observing). Although the limiting guide-star magnitude will vary with lunation, the only difference in the case where the faintest natural guide stars is  $R = 18.5$  mag (the ideal dark sky performance of GeMS) will be a higher number of pointings with low  $F$ .

The enormous benefits that emerge from observing in an AO-optimized field are obvious from even a cursory inspection of Figure 9, but it is worth discussing the figure in some detail. In analyzing this figure, we noted that even in our adaptive-optics optimized deep field (ID 8328, see Table 1), for bright time observing only about  $\sim 1\%$  of the pointings in the field fall within triangles of guide stars that are approximately equilateral (as defined above). However, if we allow any configuration of three suitably bright guide stars, sky coverage in the AODF is 55%. The

$0 \lesssim F < 20$  range in this case covers the MCAO performance when less than three natural guide stars are available. If we assume dark time observing, the sky coverage is  $\sim 92\%$  but the highest figure of merit still corresponds to the configurations of brighter ( $R \lesssim 16.5$ ) stars. In contrast to this, *none* of  $\sim 1000$  uniformly distributed pointings in the COMBO 17 Field 2 and only *one* pointing in the CFHTLS W2 subfield fell within equilateral triangles of natural guide for our simulated bright time conditions, and this fraction rises to only 0.2% (COMBO 17 Field 2) and 1.2% (CFHTLS W2) at dark time. If the MCAO requirement is relaxed to allow any configuration of three NGS, COMBO 17 Field 2 coverage is 0.4% and 3.8% for bright and dark time observing conditions, respectively. Three AO-suitable stars with  $R \lesssim 16.5$  forming a triangle were found around 1.8% of the CFHTLS W2 pointings. If the magnitude limit is lowered to  $R \lesssim 18.5$ , CFHTLS W2 coverage for sets of three stars arranged in any type of triangle reaches 21%. For both COMBO 17 and CFHTLS W2, the most common figure of merit values that emerge ( $0 \lesssim F \lesssim 20$ ) correspond

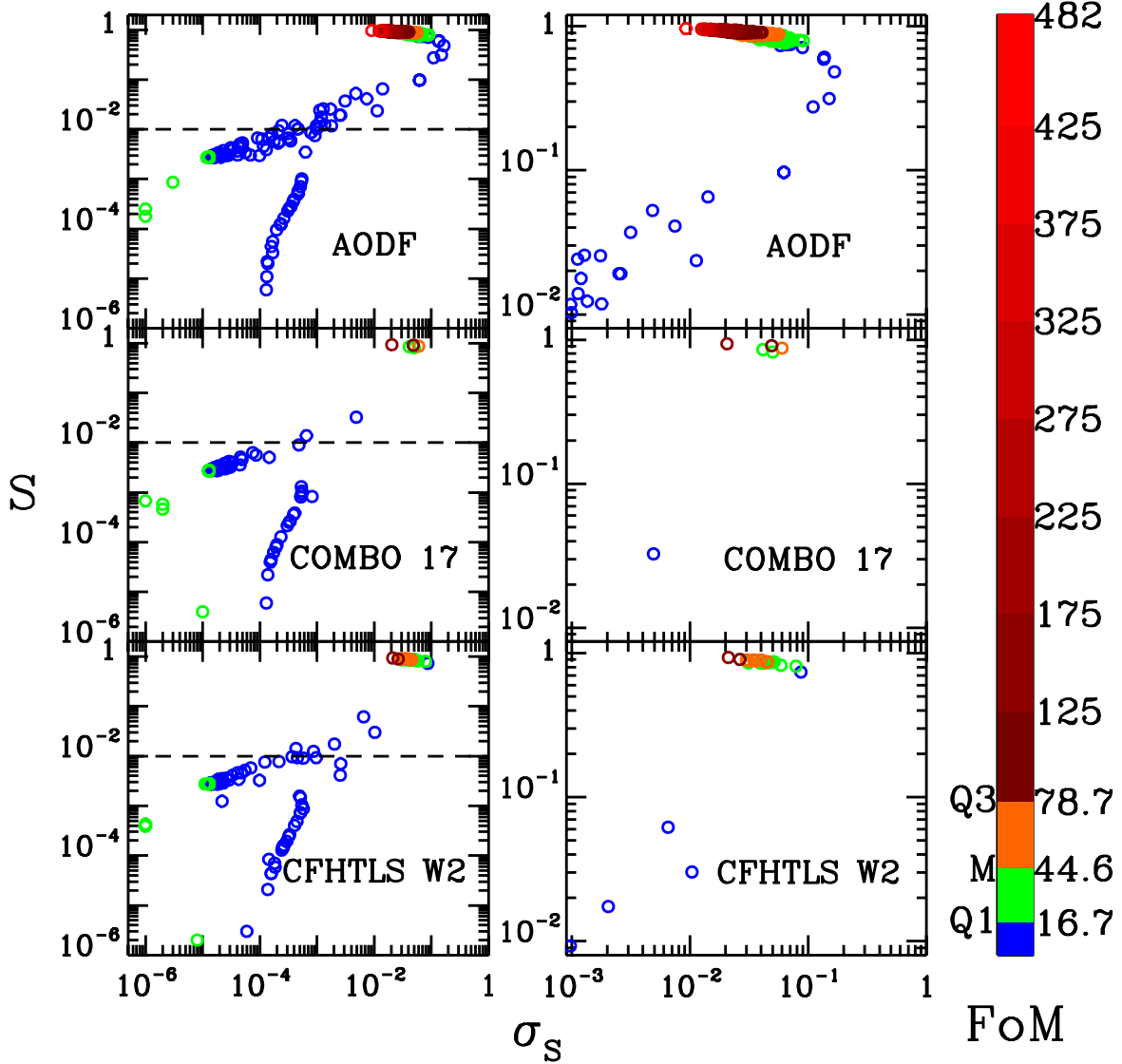


Fig. 10.— Strehl ratio as a function of its RMS variance for pointings accessible to AO in AODF, COMBO 17 Field 2, and CFHTLS W2 1 square degree subfield. Left-side panels display full range of values for Strehl ratio and its variance. The dashed line corresponds to MCAO ‘failure’ for pointings where only one or two guiding stars are available. The right-side panels show the range of Strehl ratios and related variances for pointings where MCAO is efficient (i.e., where at least one set of three AO-friendly stars forming a triangle is available). In each panel points are color-coded according to figure of merit value (equation 2). Color bar labels Q1, M, and Q3 represent the first quartile, median, and the third quartile of the figure of merit distribution across the AODF. All panels correspond to a guide star magnitude limit of 16.5 mag in  $R$ -band (the expected bright time magnitude limit for the Gemini GeMS MCAO system).

to MCAO performance with only one or two stars natural tip-tilt stars. Thus the low sky coverage in the COMBO 17 Field 2 and CFHTLS W2 sub-field results in the large spike in the first bin in Figure 9, with only a few (out of 1000) positions with high  $F$  producing a steep decline at  $F \approx 20$ . In contrast to this, the median value of  $F$  in the AO-optimized field is a factor of three higher than in COMBO 17 Field 2 and CFHTLS W2, and a significant tail of  $F$  extends out to  $F \sim 500$  (a factor of three better than the best  $F$  obtained in COMBO 17 Field 2 and CFHTLS W2 subfield).

Figure 9 shows the superiority of the AODF over both COMBO 17 Field 2 and CFHTLS W2 in terms of the figure of merit. The relation between the figure of merit values and the quantities that enter Equation 2 (the average Strehl ratio and its RMS variation over the field of view) is explored in Figure 10, where points are color-coded according to their figure of merit values. (The reader is once again reminded that the Strehl ratios in our calculations take into account only the tip-tilt correction). Dashed line in the left-hand panels denotes threshold value of the average Strehl ratio at which MCAO fails, i.e., when there are only one or two NGSs available. While  $\sim 70\%$  of the AODF pointings with available NGS have Strehl ratios above the MCAO threshold, for the COMBO 17 Field 2 and the CFHTLS W2 that fraction is 3.8% and 8%, respectively. The right-hand panels show the distribution of Strehl ratios and corresponding variances for MCAO performance when the required geometry of guiding stars is available. Figure 10 confirms that the figure of merit we have defined does rather nicely map onto fields with the combination of high average Strehl ratios *and* low RMS variation in Strehl over the  $80'' \times 80''$  field of view. The third and fourth quartile of the figure of merit distribution for the AODF (orange and red points in Fig. 10), that enclose Strehl ratios of  $90\% < \langle S \rangle < 97\%$  and RMS variations of  $1\% < \sigma_S < 6\%$ , contains only 3% of the CFHTLS W2 pointings available for AO and 1.5% of the corresponding pointings within the COMBO 17 Field 2. This hugely better AO performance clearly illustrates the benefits of undertaking extragalactic AO observations in fields optimized for adaptive optics.

### 5.3. The AODF in the era of upcoming methods and instruments

Although the MCAO has been emphasized in the present paper, other AO methods are in development especially for use with the 30m-class telescopes. These methods include multi-object adaptive optics (MOAO) and systems with faint infrared (IR) tip-tilt sensors whose images are “sharpened” by the AO system. Future AO systems are expected to be less sensitive to the (bright) NGS surface density.

MOAO (Assémat et al. 2007) is a technique that allows simultaneous AO corrections for several small IFU target fields (typically  $2 - 4''$  in diameter, sufficient to map velocity fields of large spiral galaxies at  $z \gtrsim 1$ ) within a wider field of view (FOV  $\sim 5 - 10'$ , driven by the surface density of line emitting galaxies at  $z \gtrsim 1$ ). Each IFU target field is corrected by a separate deformable mirror (DM) that provides AO correction along a given line-of-sight only (in contrast with MCAO systems that provide this correction across the whole FOV). Multiple NGS are used for tomographic wavefront sensing (Ragazzoni et al. 2000), i.e., to probe the 3D phase perturbations in the atmosphere above the telescope primary aperture. A real-time control system then slices multiple columns through the mapped turbulent volume in the directions of all targets and applies a correcting signal to multiple independent DMs. The critical difference between MOAO and MCAO is that the former is an open loop system where the wavefront sensors do not get any feedback from DMs. In other words, the wavefront error is measured and corrected only once, and the accurate system calibration is essential.

While an advantage of open-loop MOAO is that it does not need a guide star for each target, the limiting magnitude of the NGS is set by the requirement for low system error level. Thus even MOAO designed for the 30m-class telescopes will still need guide stars brighter than  $R = 17$  mag. For example, an appropriate configuration for mapping turbulent atmospheric layers using the EAGLE MOAO system that is being developed for the E-ELT involves 5 NGS with  $R < 17$  mag in the  $7'3$  patrol FOV (Rousset et al. 2010). Based on the average star counts surface density, only one out of 55 existing deep fields

mentioned earlier (COMBO 17) lies above (and very close to) this threshold. On the other hand, the number density of available NGS in the AODF is six times higher than EAGLE MOAO requirements.

As was noted earlier, as the primary mirror of a telescope becomes larger, its sensitivity allows fainter stars to be used for wavefront sensing. AO systems on 30m-class telescope will give satisfying performance with a NGS magnitude limit of  $R \approx 21$  mag (though the limiting magnitude will be lower in MOAO mode, as noted above). We performed the same analysis as in previous section on the COMBO-17 field using GeMS MCAO simulator and looked for stars arranged into triangles within magnitude range  $13 < R < 21$ , based on the USNO-B catalog (with limiting magnitude of  $R = 22$ , Monet et al. 2003). Although the sky coverage in this case is  $\sim 47\%$ , only  $\sim 15\%$  of these sets of three stars will provide Strehl ratio greater than 0.5. On the other hand, the sky coverage for high Strehl ratio values (i.e., guide stars arranged in equilateral or isosceles triangles) using MCAO system in the AODF is 100%.

Another advanced type of AO planned for 30m-class telescopes will utilize IR tip-tilt wavefront sensing. A major advantage of this approach is increased guide star density, since faint IR NGS images are sharpened by the AO system. For example, for the TMT NFIRAOS the probability of finding at least 1 tip-tilt star brighter than  $J = 21$  mag is 95% at high galactic latitude. However, at least three NGS are still required to detect the effects of tilt anisoplanatism; the use of only one off-axis tip-tilt star would give blurred time-averaged images of the science objects. This condition lowers the sky coverage that NFIRAOS will achieve to 50% at high latitudes (Wang et al. 2008). Even with three guide stars one expects to get a continuum of performance. Fainter stars will force the system to run slower which in turn leaves larger tip, tilt and focus errors. Thus, although MCAO system on a 30m-class telescope will operate over much of the sky, an insufficient number of bright guide stars will impair imaging performance, as diffraction-limited cores will be blurred out by these tip/tilt/focus errors and the variation across the FOV will be increased. (IFU work will be less affected, because the ensquared energy loss in a spaxel a few times larger than the diffraction

limit will be lower). This type of systems will give the best results when used on a field densely populated with bright NGS, where the AO is not pushing the boundaries of the control system. Finally, we note that AO using natural guiding stars only (of magnitude  $\sim 12$  and within  $\sim 15''$  of the science object) is capable of achieving higher Strehls than MCAO, is easier to do, and removes all the complications of changing plate scales, cone effect, laser elongation, etc. A major benefit of doing AO in the proposed field is that it will allow much of the of the 30m-class telescope science to be done in NGS mode. For example, if an AO system, similar to EAGLE MOAO, that uses only bright NGS were employed in the AODF, sky coverage would be  $\gtrsim 75\%$ .

We conclude this section by noting that fields optimized for ground-based adaptive optics with 30m-class telescopes will not be made obsolete by upcoming space missions, such as JWST and Euclid/WFIRST (both of which are 5–10 years away in any case). Euclid/WFIRST will likely only operate in slitless spectroscopy mode, while JWST will be equipped with a micro-shutter array for simultaneous spectroscopy of  $\sim 100$  sources and with an IFU for 3D spectroscopy, spanning the wavelength range of  $1 - 5 \mu\text{m}$  (Gardner et al. 2006). However, the main point is that the future ground-based observations will still be undertaken at spatial resolutions a factor of 5 and 15 times higher than the angular resolution of JWST and Euclid/WFIRST, respectively.

## 6. Summary and Conclusions

We have combed through stellar density and extinction maps to identify 67 low Galactic latitude fields with high star density, remarkably low extinction, relatively large area (1 square degree, to mitigate the effects of cosmic variance), and an AO-friendly stellar mix of many  $R = 13 - 16.5$  mag but few  $< 8$  mag stars. These fields allow highly efficient adaptive optics to be undertaken in low extinction extragalactic fields with minimal saturation and scattering. A comparison of these fields with existing deep fields reveals that while the number of guiding stars per square arcminute is on average 15 times higher in the AO-friendly fields, the mean level of extinction is comparable to the more extincted existing deep fields.

By augmenting our analysis with some practical considerations (such as the desire for an equatorial field accessible from both hemispheres), we identify a single one square degree field (which we designate the Adaptive Optics Deep Field, or AODF) as being particularly promising for extragalactic AO work. This field is centered at RA:  $7^{\text{h}}24^{\text{m}}3^{\text{s}}$ , Dec:  $-1^{\circ}27'15''$ . Analysis of galaxy counts in this field based on short observations of this AODF in  $g'$  and  $z'$  bands (using MegaCam on CFHT) confirm both the absence of extinction and the abundance of suitable tip-tilt stars the AODF. In fact, galaxy counts in this field closely follow the counts found in the CFHTLS Deep data set.

Simulations were undertaken to estimate the practical performance benefits of undertaking AO observations in the AODF. Our analysis shows enormous advantages emerge from undertaking AO observations in optimized fields such as the one described here. For example, for geometries of natural guide stars which produce spatially stable high Strehl ratio PSFs, dark time sky coverage in the AODF is essentially 100% using the Gemini MCAO system, which is a factor of over 50 times higher than for most existing deep fields.

## Appendices

### A. Properties of selected fields

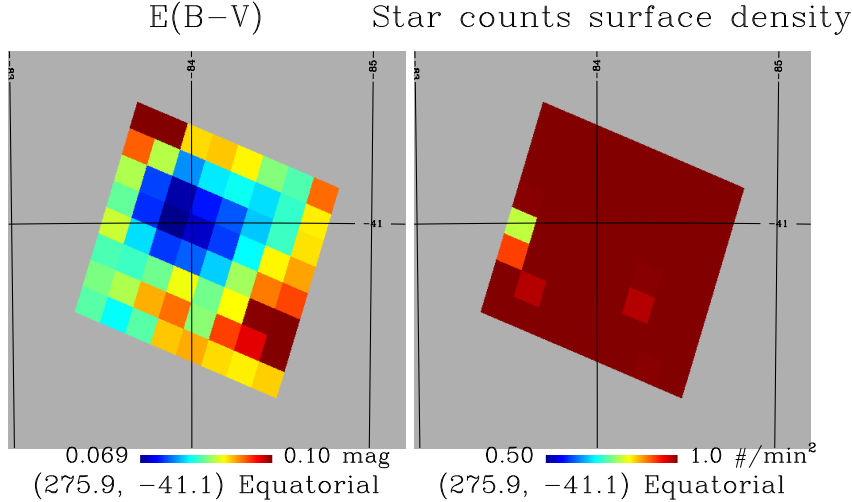


Fig. 11.— Extinction and star surface density maps of the  $6'871 \times 6'871$  cells within the  $55' \times 55'$  field with the highest mean star counts surface density of  $\langle \Sigma_{sc} \rangle = 1.3 \text{ arcmin}^{-2}$  (i.e., with 11,000 star-forming galaxies potentially observable with AO if the average number surface density of these objects is  $3 \text{ arcmin}^{-2}$ ). The field is centered at  $\alpha = 18^{\text{h}}23^{\text{m}}39^{\text{s}}53$ ,  $\delta = -41^{\circ}6'44''.3$ . Solid line grid corresponds to the celestial coordinate system with  $\text{RA}[^{\circ}] = 360^{\circ} - \alpha[^{\circ}]$ .

Figure 4 demonstrates how the set of  $55' \times 55'$  fields that are most suitable for AO observations were selected. Amongst this set we chose our preferred field (the ‘AODF’) partly on the basis of accessibility to both hemispheres. Other fields may be equally (or even more) suitable if this criterion is relaxed. A field of obvious interest is the one with the highest star count surface density. Table 1 shows that this field is located at  $\alpha = 18^{\text{h}}21^{\text{m}}57^{\text{s}}52$ ,  $\delta = -43^{\circ}14'2''.775$ . It is flagged with an open circle in Figures 4 and 8 and presented in more detail in Figure 11, where star count surface density and extinction maps with finer sampling ( $6'871 \times 6'871$ ) are used to bring out the features of individual cells within the field. The number of stars in this field is  $\sim 5000$ , corresponding to more than one star per arcminute squared.

Another property worth optimizing for is dust extinction, so it is interesting to look for fields with extraordinarily low extinction in Table 1. The field with the lowest reddening coefficient  $E(B - V)$  is centered at  $\alpha = 18^{\text{h}}30^{\text{m}}14^{\text{s}}96$ ,  $\delta = -47^{\circ}35'20''.76$  and also flagged in Figures 4 and 8. A close-up view of its stellar surface density and reddening coefficient distribution is given in Figure 12. Although this field features lower extinction than some of already explored deep fields, the number of its potential AO guiding stars is almost an order of magnitude higher than in the existing deep fields labeled in Figure 8.

Finally, it is interesting to consider fields with highly homogenous extinction. The third flagged field in Figures 4 and 8 is the one with the lowest value of standard deviation for  $E(B - V)$  from Table 1 at  $\alpha = 17^{\text{h}}40^{\text{m}}30^{\text{s}}18$ ,  $\delta = -61^{\circ}25'54''.54$ . The properties of this field’s  $6'871 \times 6'871$  cells are given in Figure 13. Despite not having the highest number of AO suitable stars ( $\gtrsim 2350$  vs.  $\gtrsim 4600$ ) or the lowest dust extinction (its  $\langle E(B - V) \rangle$  is  $\sim 35\%$  higher than in the field with minimum extinction), this field may be interesting for certain studies in which reddening homogeneity is more important than other factors.

The higher order statistical moments of star counts within sub-fields, along with proximity to other

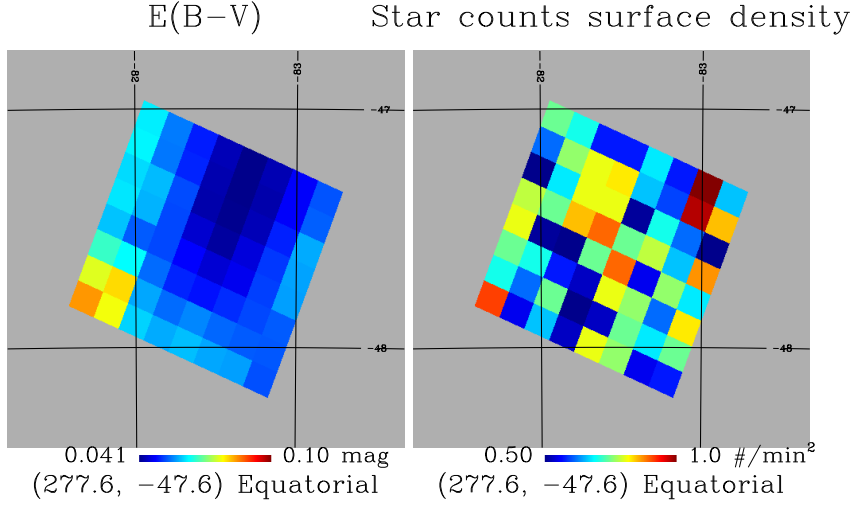


Fig. 12.— Extinction and star surface density maps of the  $6'.871 \times 6'.871$  cells within the  $55' \times 55'$  field with the lowest reddening coefficient ( $\langle E(B - V) \rangle = 0.053$  mag) but still containing more than 2500 possible guiding stars ( $\sim 5900$  observable star-forming galaxies with number surface density of  $3 \text{ arcmin}^{-2}$ ). The field is centered at  $\alpha = 18^{\text{h}}30^{\text{m}}14^{\text{s}}.96$ ,  $\delta = -47^{\circ}35'20''.76$ . Solid line grid corresponds to the celestial coordinate system with  $\text{RA}[^{\circ}] = 360^{\circ} - \alpha[^{\circ}]$ .

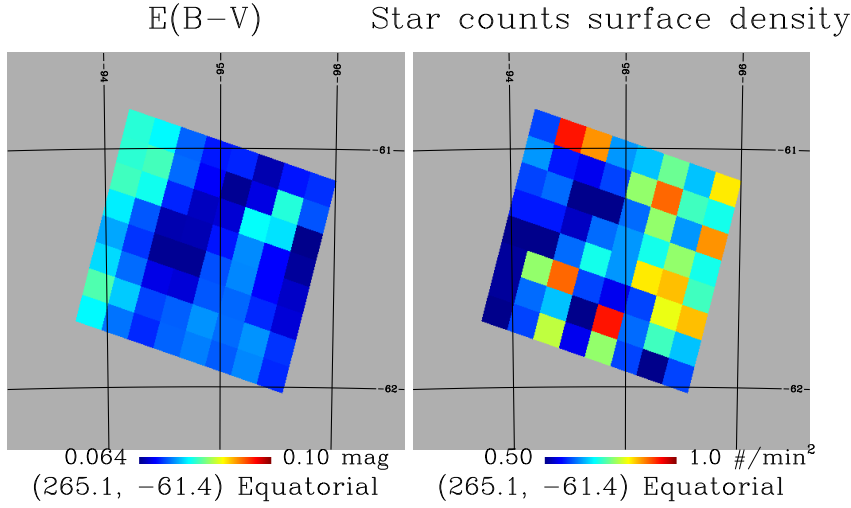


Fig. 13.— Extinction and star surface density maps of the  $6'.871 \times 6'.871$  cells within the  $55' \times 55'$  field with the lowest standard deviation of  $E(B - V)$  that translates into the smallest variation in dust content across the field. There are  $\gtrsim 2350$  13 – 16 mag stars suitable for AO guiding in the field corresponding to  $\sim 5600$  observable star-forming galaxies with the number surface density of  $3 \text{ arcmin}^{-2}$ . The field is centered at  $\alpha = 17^{\text{h}}40^{\text{m}}30^{\text{s}}.18$ ,  $\delta = -61^{\circ}25'54''.54$ . Solid line grid corresponds to the celestial coordinate system with  $\text{RA}[^{\circ}] = 360^{\circ} - \alpha[^{\circ}]$ .

suitable areas, may be other factors worth considering when choosing fields. Whether the the higher order moments really matter depends on the specific science objectives of the observations. The skewness,  $\gamma_3$ , in the star count surface density distribution might be worthwhile to consider in cases where one wishes to optimize for having a smaller number of fields with many NGS. For example,  $\gamma_3 < 0$  corresponds to the mass of distribution shifted towards higher values. For such fields there are many patches of very high star density. On the other hand, kurtosis in the  $E(B - V)$  distribuion,  $\gamma_4$ , could be important if one wishes to optimize a field for photo-z consistency. Fields with  $\gamma_4 < 0$  have a less peaked distribution of  $E(B - V)$ , i.e., more uniform extinction. The area within dashed lines in Figure 4 contains the fields from three regions in the sky. When identifying the best AO field in each region (coloured arrows in Figures 4 and 5), we have taken into account all four moments of both star counts surface density and extinction distributions. In Figure 5 we present three moments - standard deviation, skewness, and kurtosis - for all 67 fields from Table 1 as functions of the mean star count surface density (the most important factor for identifying AO-friendly fields).

## B. The form of the figure of merit

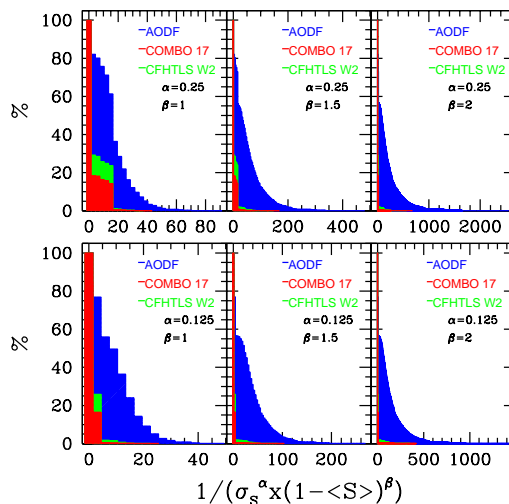


Fig. 14.— Cumulative distribution of our Strehl-related figure of merit for  $55' \times 55'$  AODF (black), COMBO 17 (red) field, and the  $1^\circ \times 1^\circ$  subfield of CFHT W2 (green). Data points are binned according to their figure of merit value in 3 (units) wide bins. Vertical axis gives the percentage of field area with the figure of merit value equal or higher than the corresponding bin's lower limit. In each panel the figure of merit is defined by different combination of the two exponents (Eq. B1). All panels correspond to a guide star magnitude limit of 16.5 mag in  $R$ -band (foreseen bright time limit for the Gemini GeMS MCAO system).

Our proposed figure of merit, given in Equation 2, is useful for characterizing AO system performance, but there is considerable flexibility in choosing the values of the exponents in this equation. We chose exponents which strike a balance between emphasizing the importance of peak Strehl ratio in a field and emphasizing the uniformity of the Strehl ratio throughout the field. Other, equally valid, choices of these exponents could be made that strike a different balance. In order to investigate how different combinations of exponents in Equation B1 might influence our general conclusions, we have defined a more generic form of the figure of merit:



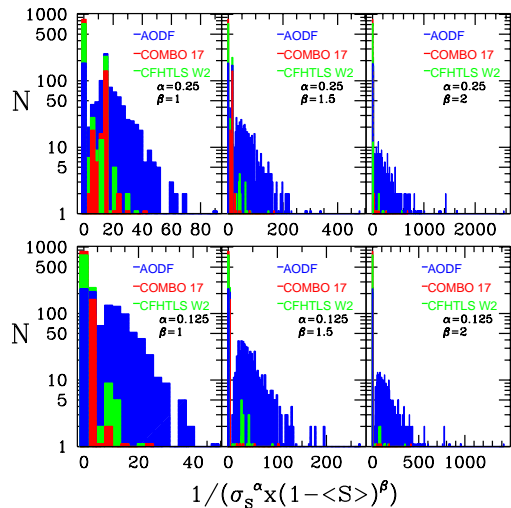


Fig. 15.— Distribution of our Strehl-related figure of merit for  $55' \times 55'$  AODF (black), COMBO 17 (red) field, and the  $1^\circ \times 1^\circ$  subfield of CFHT W2 (green). Data points are binned according to their figure of merit value in 3 (units) wide bins. Ordinate represents the number of pointings contained in individual bin. In each panel the figure of merit is defined by different combination of the two exponents (Eq. B1). All panels correspond to a guide star magnitude limit of 16.5 mag in  $R$ -band (foreseen bright time limit for the Gemini GeMS MCAO system).

$$F = \frac{1}{\sigma_S^\alpha \times (1 - \langle S \rangle)^\beta}, \quad (\text{B1})$$

where exponents  $\alpha$  and  $\beta$  can take several values:  $\alpha \in \{0.25, 0.125\}$ ,  $\beta \in \{1, 1.5, 2\}$ . The maximum image quality (i.e., average Strehl ratio) is weighted by the  $\beta$  exponent. Constraints on the range of values for  $\alpha$  are set so that the high values of the figure of merit cannot coincide with extremely low values for *both* Strehl ratio and its variance.

The resulting distributions for all six possible combinations are given in Figures 14 and 15. In this figure we have examined and compared three fields: AODF, COMBO 17, and a  $1^\circ \times 1^\circ$  subfield within CFHT W2. The corresponding histograms are presented in blue, red, and green, respectively. Of course the range of values that the figure of merit can take is seen to depend rather strongly on the choice of exponents, but the important thing to note is that none of the distributions show major changes in shape or relative position for different combinations of  $\alpha$  and  $\beta$ . Furthermore, the highest figures of merit in all six cases (for all three fields) correspond to the pointings with the highest average Strehl ratio ( $\langle S \rangle > 90\%$ ) and relatively low variation of Strehl across the  $80'' \times 80''$  field of view ( $\sigma_S \lesssim 2\%$ ). Since our analysis relies only on relative comparisons between different fields, our overall conclusions seem quite robust to the specific choices of the exponents.

## Acknowledgments

ID and RGA thank NSERC, the Government of Ontario, and the Canada Foundation for Innovation for funding. We thank Sidney van den Bergh, Chuck Steidel and Thierry Contini for interesting discussions. This work is based in part on data products produced at the TERAPIX data center located at IAP.

## REFERENCES

- Abazajian K. N., et al., 2009, *ApJS*, 182, 543
- Alcalá, J. M., et al. 2004, *A&A*, 428, 339
- Arnouts, S., et al. 2007, *A&A*, 476, 137
- Assémat, F., Gendron, E, Hammer, F. 2007, *MNRAS*, 376, 287
- Bell, E. F., et al. 2004, *ApJ*, 608, 752
- Bertin, E., et al. 2002, *Astronomical Data Analysis Software and Systems XI*, ASP Conference Proceedings, 281, 228
- Bessell, M. S. 1979, *PASP*, 91, 589
- Bonaccini, D., et al. 1999, *The Messenger*, 98, 8
- Bournaud, F., Elmegreen, B. G., Elmegreen, D. M. 2007, *ApJ*, 670, 237
- Bouwens, R. J., et al. 2010, *ApJ*, submitted (arXiv:1003.1706)
- Bouwens, R. J., et al. 2009, *ApJ*, 705, 936
- Cooper, M.C., et al. 2008, *MNRAS*, 383, 1058
- Coupon, J., et al. 2009, *A&A*, 500, 981
- Cowie, L. L.; Hu, E. M.; Songaila, A. 1995, *AJ*, 110, 1576
- Davies, R., et al. 2008, *The Messenger*, 131, 7
- Davis, M., et al. 2007, *ApJ*, 660, L1
- Dickinson, M., et al. 2003, in *The Mass of Galaxies at Low and High Redshift: Proceedings of the ESO Workshop held in Venice, Italy, 24-26 October 2001*; eds. R. Bender & A. Renzini, p. 324
- Di Matteo, P. et al. 2009, *A&A*, 499, 427
- Driver, S. P., & Robotham, A. S. G. 2010, *MNRAS*, accepted (arXiv: 1005.2538)
- Egami, E., et al. 2004, *ApJS*, 154, 130
- Ellis, R. 1997, *Ann. Rev. Astron. Astrophys.* 35, 389.
- Ellerbroek, B. L., et al. 2003, in *Adaptive Optical System Technologies II*, Proc. SPIE, 4839, 55
- Ellerbroek, B. L., & Tyler, D. W. 1998, *PASP*, 110, 165
- Eikenberry, S. S., et al. 2004, in *Ground-based Instrumentation for Astronomy*, Proc. SPIE, 5492, 1196
- Epinat, B., et al. 2009, *A&A*, 504, 789
- Erb, D. K. et al. 2006, *ApJ*, 646, 107
- Flicker, R., & Rigaut, F. 2001, in *Beyond Conventional Adaptive Optics*, ESO Conf. and Workshop Proc., 58, 377
- Flores, H. et al. 2006, *A&A*, 455, 107
- Förster-Schreiber, N. M., et al. 2009, *ApJ*, 706, 1364
- Fukugita, M., et al. 2004, *AJ*, 127, 3155
- Gardner et al. 2006, *Space Science Reviews*, 123, 485
- Górski, K. M. et al. 2005, *ApJ*, 622, 759
- Kimble, R. A., et al. 2008, in *Space Telescopes and Instrumentation 2008: Optical, Infrared, and Millimeter*, Proc. SPIE, 7010, 70101E-1
- Green, A. W., et al. 2010, *Nature*, 467, 684
- Kobayashi, C. 2004, *MNRAS*, 347, 740
- Labbé, I., et al. 2003, *AJ*, 125, 1107
- Lai, O., et al. 2008, in *Adaptive Optics Systems*, Proc. SPIE, 7015, 70154H
- Law D. R., et al. 2009, *ApJ*, 697, 2057
- Mannucci F. 2007, *Astronomy with Laser Guide Star Adaptive Optics*, <http://www.mpia-hd.mpg.de/PARSEC/Ring2007/TalksPostersPDF/Tuesday/HighzFilippoMannucci.pdf>
- McGregor, P., et al. 2004, in *Ground-based Instrumentation for Astronomy*, Proc. SPIE, 5492, 1033
- Monet, D. G., et al. 2003, *AJ*, 125, 984
- Moustakas, L. A., & Somerville, R. S. 2002, *ApJ*, 577, 1
- Ono, Y., et al. 2010, *MNRAS*, 402, 1580

- Queyrel, J., et al. 2009, *A&A*, 506, 681
- Ragazzoni, R., Marchetti, E., Valente, G. 2000, *Nature*, 403, 54
- Rigaut, F. J., et al. 2000, in *Adaptive Optical Systems Technology*, Proc. SPIE, 4007, 1022
- Rigaut, F., & Gendron, E. 1992, *A&A*, 261, 667
- Rix, H.-W. et al. 1997, *MNRAS*, 285, 779
- Rix, H.-W. ,et al. 2004, *ApJS*, 152, 163
- Roggemann, M. C., & Welsh, B. 1996, *Imaging through turbulence*, Publisher: Boca Raton, FL: CRC Press, 1996. Series: Laser and optical science and technology. ISBN: 0849337879
- Rousset, G., et al. 2010, 1st AO4ELT conference - *Adaptative Optics for Extremely Large Telescopes*, held 22-26 June, 2009 in Paris, France.; eds. Y. Clnet, J.-M. Conan, Th. Fusco, and G. Rousset, EDP Sciences, id. 02008
- Schlegel, D. J., et al. 1998, *ApJ*, 500, 525
- Scoville, N., et al. 2007, *ApJS*, 172, 1
- Shim, H., et al. 2009, *ApJ*, 696, 785
- Stiavelli, M., & Matteucci, F. 1991, *ApJL*, 377, L79
- Trenti, M., & Stiavelli, M. 2008, *ApJ*, 676, 767
- van Dokkum, P. G., et al. 2004, *ApJ*, 611, 703
- Villar, V., et al. 2008, *ApJ*, 677, 169
- Wang, L., et al. 2008, in *Adaptive Optics Systems*, Proc. SPIE, 7015, 163
- Wolf, C., et al. 2003, *A&A*, 401, 73
- Yasuda, N., et al. 2007, *AJ*, 134, 698
- Yee, H. K. C., et al. 2000, *ApJS*, 129, 475
- Zacharias, N., et al. 2004, *AJ*, 127, 3043

TABLE 1  
 PROPERTIES OF THE  $55' \times 55'$  FIELDS IDENTIFIED IN FIGURES 3 & 4

# <sup>a</sup>	$\alpha$ h m s	$\delta$ ° ' "	$\Sigma_{\text{sc}}$ min <sup>-2</sup>	$\sigma_{\Sigma_{\text{sc}}}$ min <sup>-2</sup>	$\gamma_1(\Sigma_{\text{sc}})^{\text{b}}$	$\gamma_2(\Sigma_{\text{sc}})^{\text{c}}$	$E(B-V)$ mag	$\sigma_{E(B-V)}$ mag	$\gamma_1(E(B-V))^{\text{d}}$	$\gamma_2(E(B-V))^{\text{e}}$
8273	08 01 55.8886	-14 35 51.1368	0.6529	0.1159	0.2201	-0.1935	0.0778	0.0082	0.6996	-0.3415
8276	08 05 33.3355	-14 52 48.6047	0.6648	0.1331	0.0565	-0.2372	0.0692	0.0069	0.4663	-0.6372
<b>8328</b>	<b>07 24 02.6662</b>	<b>-01 27 14.4438</b>	<b>0.7243</b>	<b>0.1199</b>	<b>0.7418</b>	<b>0.6834</b>	<b>0.0842</b>	<b>0.0116</b>	<b>0.5841</b>	<b>-0.3379</b>
16758	19 26 57.2356	-21 00 06.8527	0.6512	0.1322	0.4283	0.5339	0.0847	0.0046	-0.0902	-0.1311
16759	19 25 39.0129	-20 08 11.7480	0.6886	0.1399	0.1533	-0.1122	0.0865	0.0051	0.1163	-0.2162
16760	19 26 03.2858	-23 06 02.0956	0.6552	0.1361	0.1152	-0.6959	0.0830	0.0060	0.9076	1.2258
16807	19 13 28.5182	-33 29 53.6142	0.6836	0.1144	-0.2496	-0.1904	0.0754	0.0082	0.1264	-0.7768
16813	19 09 30.5475	-33 53 54.2514	0.6698	0.1095	0.6056	-0.2252	0.0864	0.0063	0.7165	0.3145
17007	18 45 32.0045	-44 18 15.3369	0.6625	0.1077	0.2454	0.0127	0.0689	0.0101	0.6913	-0.5662
17013	18 51 34.5808	-39 41 51.5158	0.6859	0.1354	0.4643	-0.2977	0.0791	0.0087	0.0751	-1.2020
17016	18 48 11.6290	-43 03 10.6952	0.6493	0.1335	0.3393	-0.0503	0.0782	0.0082	-0.3202	0.7728
17018	18 43 39.3947	-43 27 05.7019	0.6668	0.1345	0.5197	-0.1590	0.0778	0.0079	0.0102	-0.8005
17019	18 41 51.8111	-42 35 40.4388	0.8053	0.1637	0.7161	0.2299	0.0776	0.0120	0.4575	-1.0243
17020	18 44 35.3906	-41 20 37.7884	0.7226	0.1468	0.7250	1.1223	0.0843	0.0088	0.6999	1.2784
17021	18 42 54.1928	-40 28 59.3417	0.8050	0.1526	0.7322	0.2712	0.0815	0.0065	1.0337	0.9215
17022	18 40 08.9584	-41 44 00.6738	0.8661	0.1679	0.2980	-0.7967	0.0764	0.0052	0.1027	-0.6874
17023	18 38 30.5484	-40 52 07.4231	0.8916	0.1350	-0.0433	0.2787	0.0826	0.0084	0.6570	-0.2598
17075	18 27 58.8002	-51 47 48.6539	0.6516	0.1194	0.2052	0.3915	0.0738	0.0107	1.0010	0.0506
17077	18 29 04.8143	-49 41 42.1637	0.6572	0.1124	0.0020	-0.2874	0.0737	0.0046	0.5543	0.9716
17078	18 25 53.1372	-50 56 23.1299	0.7260	0.1587	0.1519	-0.5390	0.0728	0.0065	-0.5469	0.1232
17079	18 23 54.2239	-50 04 40.8792	0.7656	0.1402	-0.0137	-0.8646	0.0845	0.0096	-0.1007	-1.2872
17091	18 40 01.0208	-46 48 19.8550	0.7031	0.1157	0.1433	-0.0895	0.0696	0.0072	0.7903	-0.8052
17093	18 40 53.8719	-44 42 07.6520	0.6906	0.1311	-0.1203	-0.3673	0.0713	0.0081	0.4937	-0.7466
17094	18 38 04.1331	-45 57 07.0615	0.6536	0.1029	0.1297	-0.5615	0.0657	0.0101	1.1336	-0.9206
17095	18 36 12.7661	-45 05 38.2141	0.7593	0.1210	0.2531	-0.5653	0.0598	0.0056	0.5337	0.7193
17096	18 37 08.7827	-48 03 18.3032	0.7012	0.1389	0.4229	0.0800	0.0535	0.0046	0.8826	0.2867
17097	18 35 09.7115	-47 12 03.1888	0.7124	0.1380	0.4046	-0.0505	0.0557	0.0060	0.4347	-0.0656
17098	18 32 10.1262	-48 26 55.1962	0.7240	0.1214	0.1241	-0.4096	0.0649	0.0045	0.2076	-0.1427
<i>17099</i>	<i>18 30 14.9620</i>	<i>-47 35 20.7596</i>	<i>0.6929</i>	<i>0.1318</i>	<i>0.0147</i>	<i>-0.3991</i>	<i>0.0533</i>	<i>0.0081</i>	<i>0.6250</i>	<i>0.7012</i>
17100	18 33 16.4493	-46 20 31.8008	0.7921	0.1450	0.1766	-0.4501	0.0741	0.0107	0.4304	-0.6588
17101	18 31 28.6253	-45 28 45.3891	0.8453	0.1615	0.5415	-0.0136	0.0630	0.0063	0.3935	-0.4720
17102	18 28 25.4970	-46 43 31.1481	0.8691	0.1763	0.2818	-0.8206	0.0679	0.0122	-0.0426	-0.9224
17103	18 26 41.3603	-45 51 27.5153	0.7914	0.1501	0.4085	-0.2372	0.0764	0.0106	0.2804	-0.1952
17104	18 39 04.4069	-43 50 40.8234	0.7537	0.1431	0.4959	0.3473	0.0722	0.0088	-0.7946	0.6602
17105	18 37 19.8926	-42 58 59.3005	0.7498	0.1416	0.0553	0.0113	0.0795	0.0091	0.4961	-0.1894
17106	18 34 26.5970	-44 13 54.4803	0.8241	0.1198	0.1038	-0.1377	0.0679	0.0176	0.4784	-1.1006
17107	18 32 45.2756	-43 21 56.9586	0.8132	0.1411	0.1348	-0.1838	0.0671	0.0101	0.9592	1.6666
17108	18 35 40.0269	-42 07 04.1409	0.8770	0.1726	0.1150	0.3291	0.0752	0.0081	0.4070	-0.0853
17109	18 34 04.5145	-41 14 56.3333	0.8866	0.1687	0.0054	-0.4840	0.0836	0.0080	0.0681	-0.9237
17110	18 31 08.5135	-42 29 46.6791	0.8916	0.1581	0.2791	-0.0116	0.0843	0.0156	0.4232	0.1181
17112	18 29 45.8757	-44 36 45.0522	0.9283	0.1362	0.2869	-0.4116	0.0794	0.0142	0.7674	0.1725
17114	18 25 02.1950	-44 59 10.9323	0.9693	0.1778	0.0847	0.1121	0.0782	0.0067	-0.0307	-0.9453
17115	18 23 27.6851	-44 06 42.3880	0.9336	0.1587	0.2213	-0.2587	0.0824	0.0070	0.9227	1.0957
17116	18 26 34.3634	-42 52 06.7502	0.9180	0.1542	-0.0436	-0.0388	0.0807	0.0062	0.0834	0.0063
17118	18 21 57.5217	-43 14 02.7750	0.9554	0.1916	-1.0498	1.8245	0.0823	0.0109	0.3205	-0.9074
17120	18 27 07.7550	-48 50 04.1290	0.6671	0.1567	0.1793	-0.4337	0.0701	0.0102	0.3642	-0.4607
17121	18 25 16.6832	-47 58 10.7959	0.7111	0.1280	0.2671	-0.0459	0.0710	0.0084	-0.2037	-0.7853
17177	18 50 24.7353	-33 44 49.6317	1.0975	0.1658	0.4016	0.5773	0.0855	0.0122	0.8477	0.3780
17188	18 46 40.5524	-37 07 01.4218	0.8116	0.1389	0.3189	-0.1815	0.0867	0.0083	1.1766	1.7831
<i>17288</i>	<i>18 23 39.5297</i>	<i>-41 06 44.2969</i>	<i>1.2965</i>	<i>0.2105</i>	<i>-0.0562</i>	<i>-0.5628</i>	<i>0.0857</i>	<i>0.0085</i>	<i>0.2818</i>	<i>0.0993</i>
18560	17 30 04.4220	-59 55 39.3082	0.8774	0.1563	1.0359	4.7730	0.0865	0.0058	0.3543	0.7979
22659	20 34 01.8777	+18 41 40.5432	0.7140	0.1193	0.1133	-0.0646	0.0842	0.0115	0.1667	-0.8588
22665	20 30 15.9096	+18 28 26.4926	0.7461	0.1334	0.5894	0.6151	0.0764	0.0147	0.3505	-0.6854
31486	08 04 54.9932	-15 47 16.2648	0.7365	0.1243	0.4348	-0.4508	0.0674	0.0086	0.8794	-0.2353
31487	08 08 34.1773	-16 03 51.0974	0.6575	0.1107	-0.2133	0.5630	0.0789	0.0076	-0.1390	-0.8436
<i>48510</i>	<i>17 40 30.1826</i>	<i>-61 25 54.5380</i>	<i>0.6592</i>	<i>0.1329</i>	<i>0.3597</i>	<i>-0.8497</i>	<i>0.0716</i>	<i>0.0036</i>	<i>0.4596</i>	<i>0.1084</i>
48511	17 38 41.6103	-60 32 25.4590	0.7031	0.1256	-0.2966	0.1368	0.0800	0.0066	0.0875	-0.9509
48593	17 34 57.5166	-62 37 09.1809	0.6595	0.1102	-0.1926	-0.5202	0.0654	0.0046	0.6758	0.4808
48594	17 29 01.5184	-63 47 46.8549	0.6850	0.1238	0.1940	-0.5662	0.0771	0.0071	-0.0907	-0.5278
48595	17 27 18.9816	-62 53 54.7870	0.7736	0.1170	0.1161	-1.0970	0.0788	0.0062	-0.3162	-0.2015
48596	17 33 11.4505	-61 43 28.8547	0.7230	0.1231	0.2457	-0.3871	0.0760	0.0115	-0.0218	-1.5210
48597	17 31 34.0292	-60 49 38.5446	0.8235	0.1301	0.2149	-0.4993	0.0808	0.0066	-0.1810	-0.6031
48600	17 21 01.3747	-64 03 37.7765	0.6813	0.1162	0.5003	0.4488	0.0739	0.0062	0.1536	-0.7576
48610	17 00 14.0968	-68 21 58.8538	0.6641	0.1276	-0.1090	-0.6135	0.0768	0.0049	0.0170	-0.8740
48611	16 59 02.2874	-67 27 18.9130	0.6539	0.1090	0.0080	-0.6701	0.0868	0.0055	-0.5483	-0.7081
48915	16 19 26.1713	-71 39 37.6062	0.6536	0.1084	0.2919	-0.7719	0.0806	0.0088	0.9343	0.4950
48918	16 19 40.9547	-70 44 32.6440	0.6883	0.1352	0.8101	-0.0178	0.0843	0.0106	1.0809	-0.0507

<sup>a</sup> pixel number based on  $N_{\text{side}} = 64$  HEALPix partition of the sphere

<sup>b</sup> the third moment of distribution (skewness) for star counts surface density

<sup>c</sup> the fourth moment of distribution (kurtosis) for star counts surface density

<sup>d</sup> the third moment of distribution (skewness) for extinction

<sup>e</sup> the fourth moment of distribution (kurtosis) for extinction